The Effects of Concentration Intensification on Nanoparticle Synthesis

A Thesis

Presented to the Faculty of the Graduate School

of Cornell University

in Partial Fulfillment of the Requirements for the Degree of

Master of Science

by

Curtis Williamson

January 2017

ABSTRACT

Size-dependent properties define a hallmark characteristic of nanomaterials, enabling scientists and engineers to create materials with tunable properties. Yet, these size-dependent properties in a polydisperse ensemble of nanomaterials results in a distribution of properties, which is often undesirable. Realizing the promise of nanoparticle-based technologies demands more efficient, robust synthesis methods (i.e., process intensification) that consistently produce high-quality and large-quantities of nanoparticles (NPs). Traditionally, NPs are synthesized via a colloidal hot-injection reaction, in which an organic-phase reagent is rapidly injected and mixed at high temperatures to burst nucleate NPs. The temporally short and fast nature of the hot-injection method introduce stringent demands on the mixing time-scales of the reaction, a critical factor in the scaling up of nanomaterials. To address this issue, we employ the heat-up method, whereby the organic-phase precursors are mixed near room temperature and then heated past the nucleation threshold temperature. The low temperature mixing ensures mass and thermal uniformity of the reagents, reducing processing constraints. We study the NP synthesis via a heat-up method in a regime of previously unexplored high concentrations near the solubility limit of the precursors. We seek to answer the central question, how does the nano-synthetic chemistry of the heat-up method differ when concentrations are intensified? In this highly concentrated and viscous regime, we discover the NP synthesis parameters are less sensitive to experimental variability and thereby provide a robust, scalable, and size-focusing NP synthesis. Mechanistically, our investigation of the thermal and rheological properties of the colloidal mixture reveals that this high concentration regime has an approximate order of magnitude increase in solution viscosity and heat capacity, therefore reducing mass diffusion, stabilizing the reaction to perturbations, and deterring the onset of Ostwald-ripening. Compared to the conventional synthesis methods (hot-injection with dilute precursor concentration) characterized by rapid growth and low yield, we synthesize high-quality metal sulfide NPs, and demonstrate 10-1000 fold increase in NP production relative to the current field of large-scale and lab-scale efforts. The controlled growth, high yield, and robust nature of highly concentrated solutions can facilitate large-scale nano-manufacturing of NPs by relaxing synthesis requirements to achieve monodisperse products.

Table of Contents

CHAPTER 1

Published Work – The prodigious effects of concentration intensification on nanoparticle synthesis: a high-quality, scalable approach

C.B. Williamson, D.R. Nevers, T. Hanrath, R.D. Robinson, "The Prodigious Effects of Concentration Intensification on Nanoparticle Synthesis: A High-Quality, Scalable Approach," *J. Am. Chem. Soc.* **137**, 15843 (2015). ***DOI:*** *10.1021/jacs.5b10006*

Abstract: Realizing the promise of nanoparticle-based technologies demands more efficient, robust synthesis methods (i.*e.*, process intensification) that consistently produce high-quality and large-quantities of nanoparticles (NPs). We explored NP synthesis via the heat-up method in a regime of previously unexplored high concentrations near the solubility limit of the precursors. We discovered that in this highly concentrated and viscous regime the NP synthesis parameters are less sensitive to experimental variability and thereby provide a robust, scalable, and size-focusing NP synthesis. Specifically, we synthesize high-quality metal sulfide NPs (< 7% relative standard deviation for $Cu_{2-x}S$, CdS, and PbS), and demonstrate 10-1000 fold increase in $Cu_{2-x}S$ NP production (>200 g) relative to the current field of large-scale (0.1-5 g yields) and lab-scale (<0.1 g) efforts. Compared to conventional synthesis methods (hot-injection with dilute precursor concentration) characterized by rapid growth and low yield, our highly concentrated NP system supplies remarkably controlled growth rates and a ten-fold increase in NP volumetric production capacity (86 g/L). The controlled growth, high yield, and robust nature of highly concentrated solutions can facilitate large-scale nano-manufacturing of NPs by relaxing synthesis requirements to achieve monodisperse products. Mechanistically, our investigation of the thermal and rheological properties, and growth rates reveals that this high concentration regime has an order of magnitude increase in solution viscosity, reducing mass diffusion, a ~67% increase in heat capacity, stabilizing the reaction to perturbations, and the decreasing influence of Ostwald ripening.

1.1 Introduction

By virtue of their size-tunable properties and facile solution processing, colloidal semiconductor nanoparticles (NPs), or quantum dots, have garnered intensive research interest as building blocks for many applications from optoelectronics to biological imaging[11–14]. The successful commercialization of promised NP technologies hinges critically on the development of scalable fabrication methods to provide technologically-significant quantities of high-quality NPs (*i.e.*, monodisperse size and composition). In the laboratory, monodisperse colloidal NPs are typically produced by a hot-injection method, in which organic-phase reagents are rapidly injected and mixed at high temperatures (>200°C) and reacted for a short duration (< 10 min)[15–17]. This hot-injection method has played a key role in advancing NP science by providing access to a broad library of NP sizes, shapes, and compositions[1,11,12,18]. Unfortunately, high-quality NPs produced in the laboratory by hot injection result from small-scale reactions (roughly <100 mg yield[19]). A key barrier to scaling up hot injection methods is the stringent demand for rapid precursor mixing required by the rapid reaction kinetics. For larger reactor volumes mixing is slower, which introduces obvious impediments to reproducibility and control. Moreover, there is a need for efficient synthesis methods to enable economical fabrication at scale that produce high-quality NPs with high yields (>70%).

Attempts by the NP research community to resolve these scale-up challenges have led to several developments including: 1) novel precursors[1,20], 2) seeded growth[21], 3) heat-up methods[20,22,23], 4) excess metal concentrations[4,19], and 5) high solid loading[4,9,19]. For instance, recent work using novel precursors has enabled promising strides in high-quality NP synthesis and reaction control (e.g. ammonium sulfide[1,20] and thioureas[1,20]). Alternatively, using a hot injection method Cademartiri *et al.* demonstrated that high Pb precursor loading (423 g/L) can be

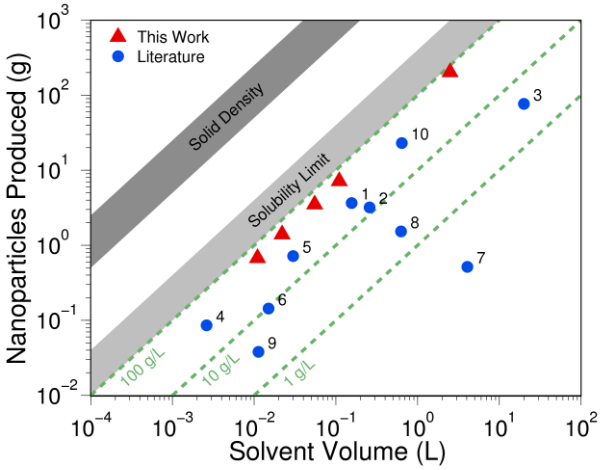

Figure 1. Scaling efforts – Comparing experiments from this work to literature reports based on the theoretical maximum possible NP yield. Production yields are depicted by the green hash-lines, and are a ratio of the full conversion of the limiting reagent to the total reaction volume. Approximate precursor solubility in long-chain organic solvents and solid precursor densities are displayed in the light and dark gray regions, respectively. Literature materials: Literature materials: 1) PbS[1], 2) Fe_2O_3[2], 3) CdSe[3], 4) PbS[4], 5) PbS[5], 6) CuS[6], 7) CISe[7], 8) CdSe[8], 9) CdSe[9], and 10) PbS[10].

used to synthesize 1.6 g of monodisperse PbS NPs (~8% size dispersion based on PL, in 50 mL reaction).[4] Although this work revealed the merit of using high precursor loading to achieve monodisperse NPs, further scale-up of this method is hindered by the need for a rapid injection and unknown kinetics of the heterogeneous reaction. Furthermore, a substantial portion of the precursor remains unreacted (and is discarded), reducing production yield (mass of NP product per reaction volume) and synthesis efficiency. **Figure 1** provides a summary of the efforts made by the NP community to scale-up NP syntheses, and a comparison to our experimental production yields reported here.

Compared to the conventional hot-injection method, the gradual heat-up synthesis offers more design flexibility and quality control, specifically for NP synthesis at large scales. The heat-up approach has already been demonstrated in the synthesis of metal oxide[16,22] and metal sulfide[10,20,24,25] NPs. Notably, some heat-up method use a "one-pot" approach, where all reagents are mixed together initially; unfortunately, this convolutes the precursors dissolution and reaction

rates, and hinders consistent production of high-quality NPs[23]. Decoupling the dissolution and reaction rates is a key "current challenge" for heat-up methods[23]. Vis-à-vis scale-up, an important advantage of the heat-up method is that precursor mixing and growth reaction are temporally decoupled; this is achieved by thoroughly mixing the precursors at low temperatures (to reduce reaction rates and enable a prolonged mixing phase), and then heating the mixed solution to initiate NP growth. To further advance the heat-up method towards large-scale synthesis, several key challenges must be resolved, namely to: 1) ensure burst nucleation during the heat-up stage, 2) control growth rates to enable size-focusing, and 3) maintain temperature uniformity through the ramp and growth stages.[23] Lastly, fine control over NP growth rates and system stability to perturbations are essential for successful scale-up.

We embraced these challenges as an opportunity to investigate a previously unexplored regime of nanoparticle synthesis: precursor concentrations near the solubility limit. We seek to answer the central question, how does the nanosynthetic chemistry of the heat-up method differ when concentrations are intensified? We find that this new regime provides a unique approach to enable a size-focusing, self-stabilizing NP synthesis. Specifically, we demonstrate that highly concentrated reagent solutions produce: (a) slow and size-focusing growth, (b) monodisperse NPs (<7%), (c) delayed Ostwald ripening, and (d) high yield. We verified the robust scalability of our process by rigorous reproducibility and spike sensitivity tests. In comparison to conventional NP synthesis (<8 g NPs/L solvent[1,2,26]), our highly concentrated heat-up method provides a ten-fold improvement in NP volumetric production capacity: 86 g/L solvent. High concentration and high precursor conversion enable process intensification: supplying efficient use of reagents, solvent, and reactor volume to produce high-quality NPs. We focus on copper (I) sulfide ($Cu_{2-x}S$) as a model system to more complex ternary copper sulfides (*e.g.*, copper indium

sulfide), which are a promising non-toxic alternative to cadmium and lead salt semiconductor NPs[27]. We also demonstrate how the highly concentrated heat-up method can be successfully generalized to PbS and CdS NPs. Through property characterization and modeling we find that this highly concentrated regime creates fortuitous synthesis conditions by providing an increase in thermal stability that absorbs temperature perturbation and a decrease in mass diffusivity that protects the system from Ostwald ripening.

1.2 Concentration Effects

To enable robust and reliable synthesis of monodisperse NPs, three conditions must be met: 1) nucleation burst, 2) size-focusing growth, and 3) delayed Ostwald ripening[16,28]. In this work we show that these conditions can be met by using a heat-up method,[20,22] and substantially increasing precursor concentrations beyond conventional NP synthesis conditions. In the discussion below, we will refer to concentrations employed in traditional NP synthesis (~100 mM) as 'conventional' in contrast to the 'highly concentrated' conditions (*i.e.*, 1000 mM) near the maximum solubility or saturation limit for the precursor in the reaction solvent. Based on a literature survey of conventional syntheses, typical precursors concentrations are one to two orders of magnitude lower, ranging from 10-100 mM (see **Table S2** for a detailed comparison).

The basic aspects of our heat-up synthesis are schematically illustrated in **Figure 2.** Organic-phase precursors are first mixed at 50˚C to ensure a uniform solution concentration and the suppression of particle growth; then, the solution is heated up to and maintained (*i.e.*, soaked) at 185˚C to grow the NPs. At the low-temperature mixing stage, both the conventional and highly concentrated reactions consist of small polydisperse NP seeds (~3 nm). However, as these seeds are heated to 185˚C, the conventional and highly concentrated conditions produce greatly

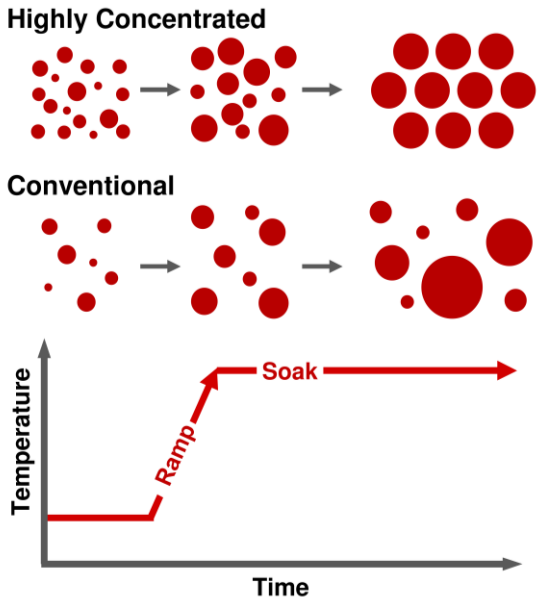

Figure 2. Reaction mechanism – Comparison of the new highly concentrated approach to the conventional NP reaction concentration using a heat-up method. Initially, both NP concentrations are the same in size and dispersion. Divergence between concentrations occurs upon soaking the NPs for an extended duration. The highly concentrated solution size focuses and become monodisperse; whereas the conventional synthesis experiences Ostwald-ripening.

divergent results: under conventional conditions the seed NPs grow into a polydisperse set, but at highly concentrated conditions the particles size-focus and become monodisperse (**Figure 2**).

The evolution of NP size and relative standard deviation (RSD) during the extended soak at 185˚C differs significantly for conventional and highly conditions (**Figure 3)**. RSD is defined as the ratio of standard deviation over mean NP diameter. To quantify the evolution of NP diameter and RSD, we extract aliquots and measure the size distribution for a large particle set (statistical NP size analysis is provided in SI-**Figure S1-2**, **Table S1**). Low concentrations (< 500 mM) yield rapid particle growth (~2.5 nm/hr) with extensive broadening of the size distribution (15-20% RSD). In contrast, more concentrated solutions (≥ 500 mM) result in significantly slower particle growth (~0.25 nm/hr) and a narrowing size distribution (7-12% RSD). Specifically, as soak time increases the conventional concentration produces NPs that continue to increase in size (5.7 nm at 0 hr to 14.7 nm at 4hr, **Fig. 3b**), while the high

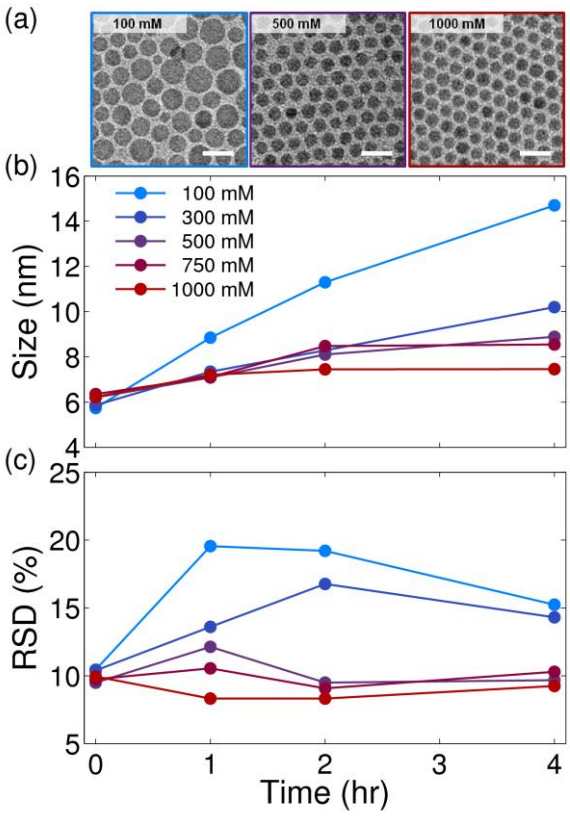

Figure 3. Effect of precursor concentration – (a) Size and relative standard deviation (RSD) of $Cu_{2-x}S$ NPs at various CuCl concentration reactions over a 4 hr soak at 185˚C. For concentrations below 500 mM, NPs experience Ostwald-ripening with time. At 500 mM and above, NP solutions are at equilibrium with a near constant size with time. (b) TEM images are color correlated to 100 mM, 500 mM, and 1000 mM reactions to illustrate size and quality. Scale bars are 20.

concentrations (≥ 500 mM) produce NPs that grow slowly (*e.g.*, 500 mM NPs are 6.2 nm at 0 hr and 8.9 nm at 4 hrs, **Fig. 3b**).

More striking is the effect of concentration on RSD: at the conventional concentration (100 mM) the RSD increases from 10% at 0 hr to 18% at 2 hrs (**Fig. 3c**), but for the concentrations ≥ 500 mM the RSD decreases; particularly for the highly concentrated solution (1000 mM), the RSD decreases from 9.6% at 0 hr to 9.8% at 2 hr (**Fig. 3c**). The 'apparent' size-focusing (decrease in RSD) for lower concentrations (< 500 mM) at longer times is an artifact of the NP size increasing faster than the absolute standard deviation, resulting in a decreasing RSD (see **Figure S2** for absolute standard deviation vs. time). Experimental data clearly illustrate that

higher precursor concentrations produce small, monodisperse particles that focus in size over extended reaction growth or soak times. The results further suggest that the crossover point for the size-focusing behavior occurs near ≥ 500 mM. Notably, the RSD achieved in this synthesis is significantly smaller than in previously reported $Cu_{2-x}S$ NPs (typically >14% RSD)[1,25,29–32]. The consistent narrow size distribution of NPs at extended soak times at 185˚C suggests that the colloidal stability of NPs fabricated by the heat-up method is greater than those fabricated by hot injection.

To explain the experimental trends observed in the heat-up synthesis we hypothesize that the nucleation and growth steps are temporally decoupled. To test this hypothesis, we extended the duration of the low-temperature (50˚C) mixing stage for 4 hr after mixing the precursors together (**Figure S3**). Both the conventional and highly concentrated reactions maintained a constant size (~3 nm) and RSD (20% RSD) during the 4 hr, indicating a stable nucleation stage at 50˚C, and the successfully the separation of nucleation and growth via the heat-up method. Further, we probe the effects of slow precursor mixing (occurring over the course of 3 min instead of instantly) and still obtain high-quality products, illustrating that our method is not dependent on a rapid injection of precursors (see **Figure S4**).

Beyond the $Cu_{2-x}S$ system, we demonstrate the general applicability of the highly concentrated heat up method to other materials, namely PbS and CdS. Similar to the $Cu_{2-x}S$ system, 1000 mM concentrations of Pb oleate and Cd oleate are mixed with a sulfur source (5000 mM sulfur oleylamine for PbS or 2500 mM tri-octyl phosphine sulfide for CdS). Identical ramp-soak heating profiles as the $Cu_{2-x}S$ system is used (ramp up to and maintain at 185˚C). For the PbS NP system, the NP size and RSD of 7.0 nm and 17.5%, respectively, experience slow growth and size-focusing throughout the 4 hour soak (size and RSD at 2 hr is 7.8 nm and 15.1%,

respectively, see **Figure S5**). Similarly, CdS NP synthesis at high concentrations has restricted growth during the long reaction duration. After 15 min into the soak, the absorbance edge does not shift, demonstrating that particle growth has ceased (see **Figure S6**). Furthermore, the full-width half-maximum of the PL for the CdS NP remain constant during the soak (FWHM of PL is 25 nm). The optically determined size and RSD are 4.8 nm and 7%, respectively. This is in close agreement with the measured size and RSD from the TEM image at 0 hr into the soak. The stabilized particle growth of PbS and CdS NPs, as well as the constant RSD, in the highly concentrated heat-up approach exhibit substantial synthesis control, which is essential to the scale-up of these materials.

1.3 Reproducibility

To characterize batch-to-batch reproducibility, we performed triplicate control experiments for the 100 mM (conventional) and 1000 mM (highly concentrated) systems under otherwise identical synthesis conditions. The average of three replicate reactions is portrayed in **Figure S7** with error bars representing the standard deviation of the size and RSD between the reactions. Replicated reactions for the conventional concentrations produce NP mean size and RSD that have considerable variations between reactions (up to ~15% variability in size and 5% variability in RSD). However, the highly concentrated reactions result in consistent sizes and RSD (< 5% variability).

1.4 Reaction Equilibrium Sensitivity

To characterize the sensitivity of the reaction equilibrium exhibited by the highly concentrated system, we perturbed the system with various chemical spikes. A 10 vol.% spike of three different chemical solutions: (1) 1000 mM dissolved copper chloride precursor, (2) 1000

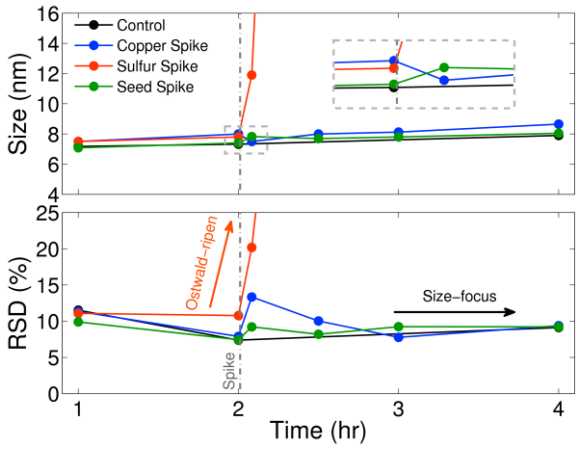

Figure 4. Reaction robustness - Concentrated reactions spiked with three different starting chemicals, 1000 mM CuCl, 1000 mM S, and 1000 mM equivalent $Cu_{2-x}S$ seeds in OLA/ODE mixture. Spike is injected after the 2 hr aliquot. The inset zooms in on the behavior of the spike: 1) copper decreases average size, 2) sulfur induces Ostwald-ripening, and 3) seeds increase average size. Spiking with Copper and Seeds leads to size focusing within 1 hr.

mM dissolved elemental sulfur precursor, and (3) ~3.0±1.0 nm $Cu_{2-x}S$ seeds (NPs from the 50˚C mixing stage). These experiments consisted of a 1000 mM medium (copper and sulfur precursors) initially mixed at 50˚C that was heated to and maintained at 185°C for 2 hours. After which, the reaction solution was spiked with one of the three spike solutions. Aliquots of each spike test were taken before the spike at zero minutes (zero is defined as the beginning of the soak phase, when the solution has just reached 185°C), 60 min, 120 min, and after the spike at 125 min (5 min post spike), 150 min (30 min post spike), 180 min, and 240 min. The size and RSD of NPs for the various spike tests is shown in **Figure 4**. The inset to **Figure 4** shows the responses to the three spikes. Notably, the highly concentrated solution quickly restores to equilibrium after chemical perturbation, via seeds or copper precursor, and is thus less susceptible to batch-to-batch chemical variations and local concentration variations within a solution.

Upon spiking the system with the copper chloride solution, a sudden decrease in the average particle size occurs with a corresponding increase in the RSD. The quality of the NPs at

five-minutes-post spike is similar to those observed at the top of the ramp (time = 0 hr). One hour after the spike, the NP distribution recovers to their original pre-spike size and RSD values. We associate this change in size and RSD with the spontaneous shift in chemical equilibrium, resulting from the etching of loosely bonded sulfur to form new seeds.

In sharp contrast to the copper chloride spike, the sulfur spike destabilizes the NP growth. We found that a sulfur spike results in a massive increase in size and RSD (**Figure 4**), both of which escalate as the soak progresses. Five minutes after the spike, the particle size and RSD doubles, and continue to ~1000 nm with ~1000% RSD by 4 hr. The sulfur spike can be viewed as a large source of anions that dampen repulsions between positively charged particles, increasing NP collisions and growth rates[33]. To understand the charge on the NPs, we measured the surface potentials of purified NPs (prior to spike) via dynamic light scattering (DLS), and the maximum surface zeta potential of our particles is approximately +50 mV. (**Figure S8**). The +50 mV is indicative of highly stabilized positively charged particles[34,35]. The large NPs resulting from the sulfur spike aggregate and precipitate out of solution, preventing a more in-depth DLS analysis. Fast particle precipitation suggests the surface potential is near 0 mV. Enhanced collisions (coalescence) reasonably explain the significant particle growth. Further, we relate the increase in sulfur concentration caused by the sulfur spike to a decrease in overall solution stoichiometry (Cu:S ratio) or sulfur rich conditions (see **Figure S9**). Reaction rich in sulfur yield extremely large (>100 nm) NPs, similar to the sulfur spike.

As a third robustness test, we also spiked the system with $Cu_{2-x}S$ seed particles (3 nm, 20% RSD), from the mixing phase at 50˚C. Upon injection of these seeds into the NP soaking solution, there is an abrupt increase in both size and RSD at 5 min after the spike. This response is not a bimodal distribution of sizes, but rather a single distribution at a slightly larger particle

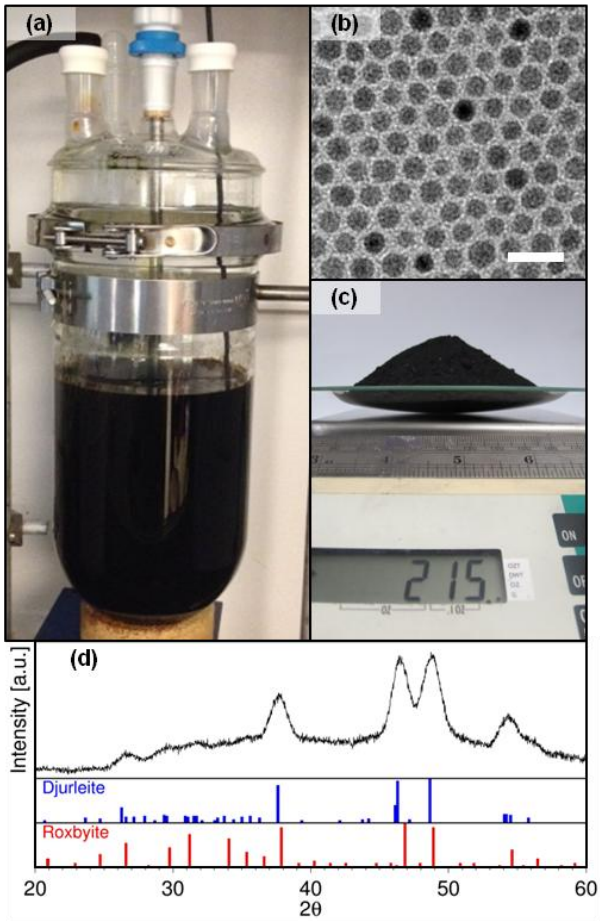

Figure 5. Large-scale reaction – (a) 2.5 L reaction of $Cu_{2-x}S$ nanoparticles. Solution is mixed via overhead stirrer at 700 rpm. (b) TEM of $Cu_{2-x}S$ nanoparticles with an average size and RSD of 8.0 nm and 9.3%, respectively. TEM images were consistent with various samplings of the final product. White scale bar on TEM image is 20 nm (c) Total recovered product of 215 g from the reaction vessel after purification and drying. (d) XRD pattern of collected NP powder. The pattern is a mix between the Djurleite ($Cu_{1.94}S$, PDF#00-023-0958) and Roxbyite ($Cu_{1.8}S$, PDF#00-023-0959) phases.

size (see inset of **Figure 4**). The rapid disappearance of the seeds after the spike implies that the injected particles had either combined with the native NPs or each other to form larger NPs.

1.5 Synthesis Scale-up

The long-time stability of NPs in highly concentrated solutions, as well as the robust system recovery from small chemical perturbations are desirable attributes for scaling up, which makes this synthesis method ideal for large scale reactions. To test this assertion, we demonstrate

the transition from a traditional lab-scale NP synthesis to a large-scale pilot reaction. We scaled a typical laboratory batch reaction volume (~25 mL) by two orders of magnitude to 2.5 L using a 4 L-reactor and an over-head stirrer with a crescent paddle blade (**Figure 5**). Following the protocol developed for small-scale reactions with the optimal highly concentrated conditions of 1000 mM CuCl and 5000 mM S, the sulfur precursor is injected into the reaction vessel containing the copper precursor at 50˚C and mixed. Similar to the small volume reactions, a 6˚C temperature spike is observed post injection, suggesting similar precursor conversion. We heat the solution to 185˚C and hold at this temperature for two hours. The reaction cools via water bath to 100˚C, at which point 2 L of ethanol quenches the solution to room temperature. The precipitated product is further purified through centrifugation.

We successfully recover 215 g of purified product. To verify batch consistency, we measure samples from six different centrifuge tubes at various purification times (TEM images provided in **Figure S10**). Sample to sample variability in the product (size and RSD) is less than 5%. The average NP size is 8.0 nm with a RSD of 9.3%. X-ray diffraction (XRD) shows the particles are mixed phase between djurleite ($Cu_{1.94}S$) and roxbyite ($Cu_{1.8}S$) phase (see **Figure 5 and S11-S12**). TGA reveals considerable mass loss at 300˚C, near the normal boiling point of oleylamine (see **Figure S13).** We associate this TGA signature with the loss of oleylamine ligand, which contributes to approximately 20 wt.% of the total collected mass. Factoring this into the theoretical conversion, we obtained a total Cu_2S conversion of greater than 93%.

1.6 Physical Properties

To understand the possible mechanisms that lead to this unexpected stability and size control at high concentrations we examine three factors that provide insight into the process at

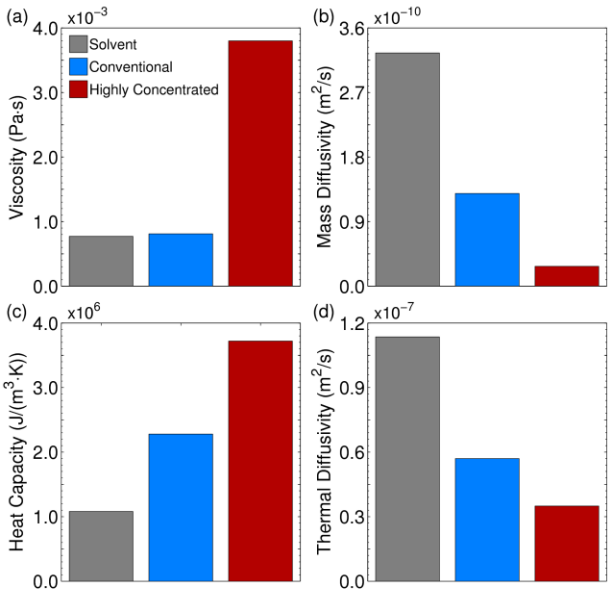

Figure 6. Experimental physical properties for conventional vs. highly concentrated NP solutions: (a) viscosity and (c) heat capacity are proportional to precursor concentration while (b) mass and (d) thermal diffusivities are inversely proportional to precursor concentration (See **SI** and **Table S3** for methods, details).

high concentrations, namely 1) the solution viscosity increases by an order of magnitude, reducing mass diffusion, 2) heat capacity increases by 67%, and 3) the decreasing influence of Ostwald ripening in NP growth. We will discuss each of these parameters in detail below.

Viscosity Effects

An important consequence of concentrating the precursor is a significant increase in viscosity of both the unreacted precursor and the reacted NP solutions. To better quantify the rheological properties of the reaction solution, we performed parallel plate rheology measurements on the NP solutions at various concentrations (see SI for details). Baseline measurements of the reaction mixture are made in reference to their organic matrix: 70% oleylamine/30% 1-octadecene. When the inorganic precursors (Cu(I)Cl and elemental sulfur) are mixed at 50˚C, both the conventional and highly concentrated solution have similar viscosities that are greater than that of the baseline of the organic matrix (see **Figure S14**). However, at

elevated temperature (120˚C), the viscosity of the conventional concentration solution (0.81 mPa·s) is similar to that of the organic matrix (0.77 mPa·s), whereas the highly concentrated solution viscosity (3.8 mPa·s) remains nearly an order of magnitude greater than the organic matrix (see **Figure 6a**). Interestingly, 500 mM corresponds to the critical turning point for both enhanced viscosity and size-focusing growth (see **Figure 3**, **S14**). The measured increase in solution viscosity with salts has been previously observed for NP containing systems, namely polymer NPs and oxide NP suspensions[36,37]. Dissociating salts present in colloidal solutions induce various electrostatic forces on the suspended NPs that inhibit the molecular transport of fluid around these particles and thus increase the solution viscosity. Unlike these NP containing solutions with salts, our solution is organic and reactive, in which the salts are our precursors. We hypothesize that the increased viscosity for highly concentrated solutions are induced by electrostatics and metal-π interactions (equivalent to H-bonding in aqueous systems) generated by the high chloride concentration and lone pair electrons (amines) within the solution.

In context of NP motion through the reaction fluid, the viscosity (μ) can be translated to mass diffusivity (D) using the Stokes-Einstein-Sutherland equation (*i.e.*, $D=k_BT/6\pi\mu r$) for NPs with a hydrodynamic radius, r. Comparing mass transport for concentrated and conventional conditions therefore shows that diffusivity in the highly concentrated condition is approximately five-fold lower, given the differences in viscosity discussed above (**Figure 6b** and **Table S3**). We therefore conclude that the reduced NP mobility in the concentrated reaction environment contributes significantly to the stability of the size distribution due to decreased NP collision rates (*see growth mechanism section below*).

Heat Transport

Thermal conductivity and heat capacity can have a significant impact on NP reactions, especially since both factors depend on NP concentration[38–40]. However, the impact of the thermal properties of the reaction fluid has not received the appropriate consideration in previous studies. We hypothesize that the higher heat capacity of the highly concentrated system renders it more robust relative to experimental thermal fluctuations. To test this hypothesis we deliberately perturbed the reaction environment (maintained at 185˚C) with a spike of solvent at room temperature. As detailed in the supporting information (**Figure S15**) thermal fluctuations due to the spike are less pronounced in the concentrated system compared to those for the conventional conditions. The immediate temperature drop in the highly concentrated reaction is roughly half that of the conventional reaction, indicating that the former has a higher heat capacity and thus a smaller thermal diffusivity. This behavior agrees with the higher heat capacity and lower thermal diffusivity measured for the highly concentrated solution (**Figure 6c-d**, **Table S3**).

1.7 Growth Mechanism

To better understand the growth mechanism we can examine the precursor conversion rate and growth models on coalescence (or agglomeration) and Ostwald ripening. The precursor conversion is assessed through the dried NP mass, while excluding the mass of organic ligands as determined by TGA (see **SI** for details, **Figure S16**). At the beginning of the soak stage at 185˚C (time = 0 hr), the conversions are near complete for both the conventional and highly concentrated conditions (82% and 88%, respectively); further, both conditions have similar sized NPs (~6 nm). The high conversion values indicate the concentration of remaining active growth species (or residual precursor) is small. Specifically, if all of the residual precursor is considered to be in the form of Cu_2S monomer, the approximate residual concentration would be 8 and 50 mM residual Cu_2S for the conventional and high concentrated solutions, respectively. In relation

to the LaMer model, the fact that the conventional conditions undergo Ostwald ripening (to be discussed, see **Figure 7**) suggests that this solution is near the monomer saturation limit (at approx. 8 mM Cu_2S monomer, **Table S4**) and that the residual monomer is in equilibrium with the monomer attached to NP surface[16,41]. Thus, the highly concentrated solution, with higher residual monomer concentration (approx. 50 mM), is still supersaturated, and resistant to Ostwald ripening[4,41].

To describe the NP size evolution during the soak stage, we calculate the increase in NP size if all of the residual precursor were to be added as new material to the existing NPs (*i.e.*, 100% conversion). The mean NP size increases by only ~7% for the conventional case (~6 nm to 6.4 nm), and ~4% for the highly concentrated case (~6 nm to 6.3 nm) (see **SI**). However, experiments show that the final size for conventional and highly concentrated (14.7 and 7.5 nm, respectively) is much greater than the size predicted by this simple calculation; this comparison indicates that another mechanism beyond monomer addition via unreacted precursor is required to describe the observed NP growth.

In light of the depleted monomer condition, we infer that the growth mechanism should be Ostwald ripening or NP coalescence, which would be governed by NP mobility or diffusivity rather than concentration gradients. Ostwald ripening is NP growth via NP dissolution to monomer, and then monomer deposition onto larger NP[16,41]. One method to assess the growth process is to plot the time evolution of volume normalized by the final volume[42,43]. For the conventional concentrations, although the growth in particle size slows as the reaction progresses, the volumetric growth rate remains fairly constant over the duration of the experiment (**Figure 7a**, blue points, 100 mM). Linear volumetric growth rate is indicative of Ostwald ripening, as supported by the Lifshitz–Slyozov–Wagner (LSW) theory[41,43–45]. Alternatively, a sigmoidal

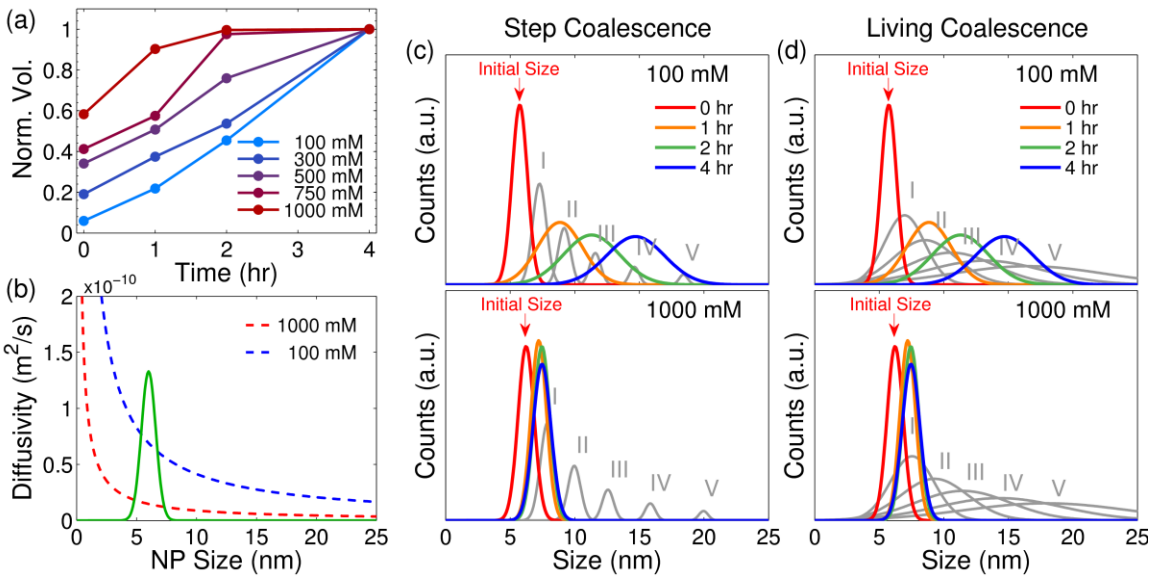

Figure 7. (a) Plots of the volumetric growth rate. The NP sizes for each concentration are converted to volume and normalized by the 4 hr "final" volume. Linearly increasing volume with time indicates Ostwald ripening, where a sigmoidal dependence suggests coalescence or monomer addition. (b) The change in Stokes-Einstein diffusivity over various particle sizes at a constant solution viscosity for the 100 and 1000 mM reaction. The average initial size distribution for both concentrations is overlaid. The diffusivity in the 100 mM reaction is five times greater than the diffusivity in the 1000 mM reaction with the same NPs. (c-d) (color curves) Mapping of the temporal evolution (0-4 hrs) of experimentally determined values, expressed as Gaussians of the mean size and SD of the conventional (top) and highly concentrated (bottom) reactions. (gray curves) I-V correspond to a projection of the system after coalescence events, with each curve progression marking a halving of the number of particles from the previous cure (e.g., condition II has half the particles of condition I, and III half that of II). (c) Step coalescence represents an aggregation mechanism where each particle must coalesce once before any particle can coalesce twice while (d) living coalescence represents a mechanism where some particles experiencing multiple coalescence events while others experience none.

curve describes the highly concentrated condition (**Figure 7a**, red points, 1000 mM), suggesting the growth process is through coalescence or monomer addition[42,43].

Additionally, LSW theory correlates the volumetric growth rate of NPs to their diffusivity, in which greater particle diffusivity induces faster growth. We determined the diffusivity of our NPs via the Stokes-Einstein-Sutherland relation (*vide supra*)[33] (See **SI**). **Figure 7b** shows the diffusivity of the conventional and highly concentrated reaction at various sizes with a constant viscosity. A Gaussian distribution of the experimentally-determined particle size and deviation is overlaid (**Fig. 7b**, green curve) on these diffusivities and represents the size and

standard deviation (SD) of both concentrations at the beginning of the soak. Interestingly, the conventional reaction has a five-fold greater diffusivity compared to the highly concentrated, at the beginning of the soak. Furthermore, the variation in particle diffusivity for an identical NP size distribution is five-fold larger in the conventional reaction. For instance, a 3-σ (3-SD) particle spread (99.7% of total particles) corresponds to variation or disparity in diffusivity of 4.55×10^{-11} $m^2 s^{-1}$ for the conventional reaction; whereas the highly concentrated reaction only varies in diffusivity by 9.70×10^{-12} $m^2 s^{-1}$ for the same NP size distribution. The higher diffusivities coupled with a larger variation in diffusivity over the particle distribution provide mechanistic insight into not only the faster particle growth of the conventional reaction, but also for its observed increase in RSD (**Figure 3**, **7a**). Moreover, as the soak time increases and the NPs in the conventional condition grow in size, their diffusivity and variation in diffusivity decrease, resulting in slower growth and a constant but large SD (**Figure 3**, **7b**).

Growth Models

We investigated various growth models to describe the growth process for each concentration. Each model represents the data to a moderate degree of accuracy (see **Table S5** for R^2 values). A model proposed by Huang *et al.*[46] suggests a two-term, three-fitting parameter model, in which the first fitting parameter (k_1) describes orientated attachment (OA) and captures the initial sigmoidal growth behavior and the second fitting parameter (k_2) describes Ostwald ripening (OR) (**Figure S17**). The third parameter (n) is an arbitrary constant that scales the time dependence on Ostwald ripening. The fits for this model generally follow the suspected trends from our data: k_2 (OR) dominates at lower concentrations, whereas k_1 (OA) dominates in the highly concentrated case. Additionally, the calculated R^2 values are near unity for each

concentration, which suggests the fits are accurate. However, the trends begin to deviate from the experimental data at the longer soak times (see **Figure S17**).

Kinetic growth profiles of NPs can also be described by the Kolmogorov-Johnson-Mehl-Avrami (KJMA) model, (**Figure S18**)[47–51] which requires the normalization of the NP volumes, such that the bounds of the expression are between 0 and 1. Unlike the Huang model, this is a two-parameter fitting model that does not describe Ostwald ripening, but rather only aggregative NP growth (k_g) or coalescence[47,48]. The growth rate increases with concentration, suggesting coalescence is as the dominant process at high concentrations, which agrees with the oriented attachment rate of the Huang model (see **Figure S18**). Lastly, we analyze our NP growth in context of the four-step NP agglomeration described by Finney *et al.*[42] Briefly, this model describes the evolution of particle size in context of rates for bimolecular agglomeration (k_3) and autocatalytic agglomeration (k_4)[42]. This agglomeration (or coalescence) model provides a good fit to the experimentally observed particle size evolution shown in **Figure 3** (see **Figure S19**). Notably, this analysis shows $k_4>k_3$ at conventional concentrations, and a transition to $k_4<k_3$ at high concentrations (see **Figure S19**). This model indicates that conventional concentrations are dominated by autocatalytic agglomeration or Ostwald ripening whereas at high concentrations, the NP synthesis is dominated by bimolecular agglomeration or coalescence. Importantly, the reduced overall agglomeration can be explained by two key experimental trends discussed above, namely: (1) higher residual precursor concentration stabilizes the NP surface and thereby reduces the energetic driving force for agglomeration and (2) the rate of NP collisions per particle is reduced in the high viscosity of the synthesis environment increases. Ultimately, these growth models each suggest the same conclusion: conventional conditions grow via Ostwald ripening,

and as the concentration increases Ostwald ripening is suppressed. Further, the models indicate the growth mechanism for high concentration is via coalescence.

Coalescence Modeling

To determine the magnitude of growth by coalescence, we compare the theoretical evolution in size distribution for NPs undergoing coalescence to our experimentally measured size distributions. Specifically, as an analogy to polymerization chemistry, two theoretical types of coalescence processes are considered: step coalescence and living coalescence (see **SI** for model details). Step coalescence means that each particle must coalesce once before any particle can coalesce twice (or again). This would allow the NPs in solution to follow similar growth trajectories and enables the NPs to equilibrate before the next coalescence step, thereby reducing the RSD (**Figure 7c**, gray curves). On the other hand, living coalescence means some particles may experience multiple coalescence events while others experience none. Hence, each particle experiences different growth trajectories, which consequently increase the RSD (**Figure 7d**, gray curves). Conceptually, living coalescence dominates when the probability of NP collisions is high, favoring multiple coalescence events involving the same particle. In contrast, step coalescence dominates when the probability that a particle experiences multiple coalescence events for a given time is low. **Figure 7c-d** illustrates the theoretical evolution of both step and living coalescence processes compared to our experimental data. Each shift in theoretical size distribution (*e.g.*, I→II→III, gray curves) represents the system after the number of particles has been cut in half (*e.g.*, condition II has half the particles of condition I, and III half that of II, see **SI** for details). For step coalescence, this means each particle experiences one coalescence event between I and II while for living coalescence each particle may experience a range of coalescence events. Thus, each NP involved in step coalescence follows a consistent reaction

profile or experiences the same number of coalescence events, which promotes a uniform size distribution. The opposite is true for living coalescence. Comparing our data to these theoretical distributions suggests that conventional conditions are better described by living coalescence, whereas high concentrations are better described by step coalescence (see **Figure 7c-d**).

Physically, the larger NP mass diffusivities for the conventional reactions enable some NPs to experience multiple coalescence events while other NPs in the system experience few or none, promoting a range of NP growth trajectories and increasing RSD. In contrast, NPs in high concentration reactions diffuse more slowly, experience fewer and similar numbers of coalescence events, and thus remain monodisperse. This physical insight agrees with the relative collision rate for NPs in solution. Specifically, the total collision rates are similar for both conventional and highly concentrated conditions (see **Table S4**) since the order-of-magnitude higher diffusivity in the former is offset by the order-of-magnitude lower NP concentration. Yet, the relative collision rate (or the fraction of particles that collide, *i.e.* the ratio of collision rate to the total number of particles) is near a factor of 6 higher for the conventional compared to the highly concentrated condition (see **Table S4)**. The greater number of NPs undergoing coalescence events for conventional condition supports the living coalescence process dominated by multiple coalescence events. In contrast, fewer NPs are involved in coalescence events for the high concentrations, promoting a step coalescence mechanism, more consistent reaction profiles per particle, and thus more uniform size distribution.

1.8 Conclusion

We have shown that by concentrating precursor solutions near the solubility limit it becomes possible to separate precursor mixing and NP growth, and reproducibly achieve

monodisperse NPs with a heat-up method. Within this new highly concentrated and viscous regime**,** synthesis parameters become less sensitive to experimental variability and thereby provide a reproducible and robust NP synthesis methodology. We demonstrated the intrinsic robustness of the method by showing that the NP synthesis is insensitive to chemical spikes (copper chloride and $Cu_{2-x}S$ seeds), which agree with equivalent shift in the initial precursor ratios. Encouraged by the high degree of reproducibility and robustness of the highly concentrated reaction regime, we successfully scaled the reaction two orders of magnitude in volume to 2.5 L; all while maintaining a NP size and RSD similar to that observed on the lab scale. Importantly, the scale-up to a 215 g NP batch was accomplished with an unprecedented yield of 86 grams per liter of reaction volume. Further, this method can be successfully adapted to other metal sulfides such as CdS and PbS. Our advances in the robust scale-up of colloidal NP synthesis derive from improved understanding of the interplay between chemical, thermal and rheological properties on basic nucleation and growth. We point to the heat-up method under highly concentrated reaction environments as a promising NP synthesis methodology with significant potential to resolve outstanding challenges in producing NP materials at scales and capable of meeting their emerging demand.

1.9 References

(1) Hendricks, M. P.; Campos, M. P.; Cleveland, G. T.; Plante, I. J.; Owen, J. S. *Science.* **2015**, *348*, 1226–1230.

(2) Park, J.; An, K.; Hwang, Y.; Park, J.-G.; Noh, H.-J.; Kim, J.-Y.; Park, J.-H.; Hwang, N.-M.; Hyeon, T. *Nat. Mater.* **2004**, *3*, 891–895.

(3) Kim, J. I.; Lee, J.-K. *Adv. Funct. Mater.* **2006**, *16*, 2077–2082.

(4) Cademartiri, L.; Bertolotti, J.; Sapienza, R.; Wiersma, D. S.; von Freymann, G.; Ozin, G. A. *J. Phys. Chem. B* **2006**, *110*, 671–673.

(5) Yuan, M.; Kemp, K. W.; Thon, S. M.; Kim, J. Y.; Chou, K. W.; Amassian, A.; Sargent, E. H. *Adv. Mater.* **2014**, *26*, 3513–3519.

(6) Du, Y.; Yin, Z.; Zhu, J.; Huang, X.; Wu, X.-J.; Zeng, Z.; Yan, Q.; Zhang, H. *Nat. Commun.* **2012**, *3*, 1177.

(7) Kang, X.; Yang, Y.; Huang, L.; Tao, Y.; Wang, L.; Pan, D. *Green Chem.* **2015**, *17*, 4482–4488.

(8) Protière, M.; Nerambourg, N.; Renard, O.; Reiss, P. *Nanoscale Res. Lett.* **2011**, *6*, 472.

(9) Flamee, S.; Cirillo, M.; Abe, S.; De Nolf, K.; Gomes, R.; Aubert, T.; Hens, Z. *Chem. Mater.* **2013**, *25*, 2476–2483.

(10) Zhang, J.; Gao, J.; Miller, E. M.; Luther, J. M.; Beard, M. C. *ACS Nano* **2014**, *8*, 614–622.

(11) Park, J.; Joo, J.; Kwon, S. G.; Jang, Y.; Hyeon, T. *Angew. Chem. Int. Ed. Engl.* **2007**, *46*, 4630–4660.

(12) Talapin, D. V; Lee, J.-S.; Kovalenko, M. V; Shevchenko, E. V. *Chem. Rev.* **2010**, *110*, 389–458.

(13) Kovalenko, M. V; Manna, L.; Cabot, A.; Hens, Z.; Talapin, D. V; Kagan, C. R.; Klimov, X. V. I.; Rogach, A. L.; Reiss, P.; Milliron, D. J.; Guyot-sionnnest, P.; Konstantatos, G.; Parak, W. J.; Hyeon, T.; Korgel, B. a; Murray, C. B.; Heiss, W. *ACS Nano* **2015**, *9*, 1012–1057.

(14) Sun, L.; Choi, J. J.; Stachnik, D.; Bartnik, A. C.; Hyun, B.-R.; Malliaras, G. G.; Hanrath, T.; Wise, F. W. *Nat. Nanotechnol.* **2012**, *7*, 369–373.

(15) Owen, J. S.; Chan, E. M.; Liu, H.; Alivisatos, A. P. *J. Am. Chem. Soc.* **2010**, *132*, 18206–18213.

(16) Kwon, S. G.; Hyeon, T. *Small* **2011**, *7*, 2685–2702.

(17) Murray, C. B.; Noms, D. J.; Bawendi, M. G. *J. Am. Chem. Soc.* **1993**, *115*, 8706–8715.

(18) Murray, C. B.; Kagan, C. R.; Bawendi, M. G. *Annu. Rev. Mater. Sci.* **2000**, *30*, 545–610.

(19) Weidman, M. C.; Beck, M. E.; Hoffman, R. S.; Prins, F.; Tisdale, W. A. *ACS Nano* **2014**, *8*, 6363–6371.

(20) Zhang, H.; Hyun, B.-R.; Wise, F. W.; Robinson, R. D. *Nano Lett.* **2012**, *12*, 5856–5860.

(21) Perera, S. D.; Zhang, H.; Ding, X.; Nelson, A.; Robinson, R. D. *J. Mater. Chem. C* **2015**, *3*, 1044–1055.

(22) Kwon, S. G.; Piao, Y.; Park, J.; Angappane, S.; Jo, Y.; Hwang, N.-M.; Park, J.-G.; Hyeon, T. *J. Am. Chem. Soc.* **2007**, *129*, 12571–12584.

(23) van Embden, J.; Chesman, A. S. R.; Jasieniak, J. J. *Chem. Mater.* **2015**, *27*, 2246–2285.

(24) Joo, J.; Na, H. Bin; Yu, T.; Yu, J. H.; Kim, Y. W.; Wu, F.; Zhang, J. Z.; Hyeon, T. *J. Am. Chem. Soc.* **2003**, *125*, 11100–11105.

(25) Zhang, H.-T.; Wu, G.; Chen, X.-H. *Langmuir* **2005**, *21*, 4281–4282.

(26) Jasieniak, J.; Bullen, C.; Van Embden, J.; Mulvaney, P. *J. Phys. Chem. B* **2005**, *109*, 20665–20668.

(27) Kruszynska, M.; Borchert, H.; Parisi, J.; Kolny-Olesiak, J. *J. Am. Chem. Soc.* **2010**, *132*, 15976–15986.

(28) Rempel, J. Y.; Bawendi, M. G.; Jensen, K. F. *J. Am. Chem. Soc.* **2009**, *131*, 4479–4489.

(29) Luther, J. M.; Jain, P. K.; Ewers, T.; Alivisatos, A. P. *Nat. Mater.* **2011**, *10*, 361–366.

(30) Lotfipour, M.; Machani, T.; Rossi, D. P.; Plass, K. E. *Chem. Mater.* **2011**, *23*, 3032–3038.

(31) Saldanha, P. L.; Brescia, R.; Prato, M.; Li, H.; Povia, M.; Manna, L.; Lesnyak, V. *Chem. Mater.* **2014**, *26*, 1442–1449.

(32) Leidinger, P.; Popescu, R.; Gerthsen, D.; Lünsdorf, H.; Feldmann, C. *Nanoscale* **2011**, *3*, 2544–2551.

(33) Russel, W. B.; Saville, D. A.; Schowalter, W. R. *Colloidal Dispersions*; Cambridge University Press: New York, 1989.

(34) Hanaor, D.; Michelazzi, M.; Leonelli, C.; Sorrell, C. C. *J. Eur. Ceram. Soc.* **2012**, *32*, 235–244.

(35) Xu, R.; Wu, C.; Xu, H. *Carbon N. Y.* **2007**, *45*, 2806–2809.

(36) Ogawa, A.; Yamada, H.; Matsuda, S.; Okajima, K.; Doi, M. *J. Rheol. (N. Y. N. Y).* **1997**, *41*, 769.

(37) Srivastava, S.; Shin, J. H.; Archer, L. a. *Soft Matter* **2012**, *8* (15), 4097.

(38) Chieruzzi, M.; Cerritelli, G. F.; Miliozzi, A.; Kenny, J. M. *Nanoscale Res. Lett.* **2013**, *8*, 448.

(39) Xuan, Y.; Roetzel, W. *Int. J. Heat Mass Transf.* **2000**, *43*, 3701–3707.

(40) Xuan, Y.; Li, Q. *Int. J. Heat Fluid Flow* **2000**, *21*, 58–64.

(41) Talapin, D. V.; Rogach, A. L.; Haase, M.; Weller, H. *J. Phys. Chem. B* **2001**, *105*, 12278–12285.

(42) Finney, E. E.; Shields, S. P.; Buhro, W. E.; Finke, R. G. *Chem. Mater.* **2012**, *24*, 1718–1725.

(43) Wang, F.; Richards, V. N.; Shields, S. P.; Buhro, W. E. *Chem. Mater.* **2014**, *26*, 5–21.

(44) Lifshitz, I. M.; Slyozov, V. V. *J. Phys. Chem. Solids* **1961**, *19*, 35–50.

(45) Wagner, C. *Z. Elektrochem.* **1961**, *65*, 581–594.

(46) Huang, F.; Zhang, H.; Banfield, J. F. *J. Phys. Chem. B* **2003**, *107*, 10470–10475.

(47) Shields, S. P.; Richards, V. N.; Buhro, W. E. *Chem. Mater.* **2010**, *22*, 3212–3225.

(48) Burbelko, A. A.; Fraś, E.; Kapturkiewicz, W. *Mater. Sci. Eng. A.* **2005**, 413-414, 429–434.

(49) Avrami, M. *J. Chem. Phys.* **1941**, *9*, 177.

(50) Avrami, M. *J. Chem. Phys.* **1940**, *8*, 212.

(51) Avrami, M. *J. Chem. Phys.* **1939**, *7*, 1103.

CHAPTER 2

Current Work – Diffusionless transformation, reversible atomic restructuring of cadmium sulfide magic-size cluster

Abstract: In this chapter, we analyze the nucleation step of a cadmium sulfide nanoparticle synthesis to understand the effects of high precursor concentrations. Ultra-pure magic-sized clusters (MSCs) can be directly synthesized at high concentration that exhibit behavior contradictory to common belief. When MSCs synthesized under dilute conditions (or any nanomaterial) are heated in alcohol or straight oleic acid, they continuously grow into larger particles. There is no growth with the highly concentrated MSCs, only a transformation of the family. Alcohol exposures to the MSCs induce a discrete shift in the exciton of a 324 nm family to a 313 nm family. This transformation can be completely reversed by heating the 313 nm family in oleic acid. During these transformations, there is no continuous growth of the MSC. We speculate the discrete shifting between the excitonic peaks to be a diffusionless transformation. To identify the nature of these transformations, we employ a variety of spectroscopic techniques to probe the composition, surface, and core of these MSCs. We find our cluster have a cadmium to sulfur ratio of 1.8 to 1, respectively. Analysis of the XPS indicates 25% and 40% of the cadmium atoms are on the surface of the 324 nm and 313 nm family, respectively. Using FTIR, we identify the ligand binding configuration to be suggestive of chelating bidentate for the 324 nm family and bridging bidentate for the 313 nm family. Total xray scattering experiments identify shifting in the atomic positions of the MSC core.

2.1 Motivation

Size-dependent properties define a hallmark characteristic of quantum dots (QDs). The size-dependence allows scientists and engineers to create materials with tunable properties; yet, the size-dependent properties in a polydisperse ensemble of QDs results in a distribution of properties, which is often undesirable. Current methods have yet to produce ultrasmall (<2 nm) QDs in high purity and thus its true composition, structure, and physical properties remain enigmatic. In this chapter, we identify these ultrasmall species as magic-size clusters (MSCs). A MSC family is identified by a very strong and narrow exctionic peak at specific wavelengths[1].

To identify the enigmatic properties of these ultrasmall QDs, we employ the highly concentrated heat-up method to isolate these MSCs through separation of the nucleation step and particle growth of classical synthesis. We identify distinct differences in the stability of the MSCs produced at different concentration. We find the high concentration synthesis of MSCs to be resilient to large changes in the precursor ratio. In contrast, the preparation of the precursor strongly affects the quality of the MSCs produce at dilute concentration. We further test the stability of the MSCs at dilute and high concentration by soaking the MSCs in alcohols at elevated temperature. The MSCs from the high concentration synthesis undergo a reversible transformation of its exciton; whereas the MSCs of the dilute synthesis grow into large polydisperse nanoparticles. By using this enhanced stability and purity of MSCs synthesized at high concentration, we can identify the composition and structure of this material.

2.2 Synthesis of magic-sized cluster

Ultra-pure cadmium MSCs are synthesized using high concentrations to separate particle nucleation from particle growth. We have adapted the synthesis from chapter 1, whereby

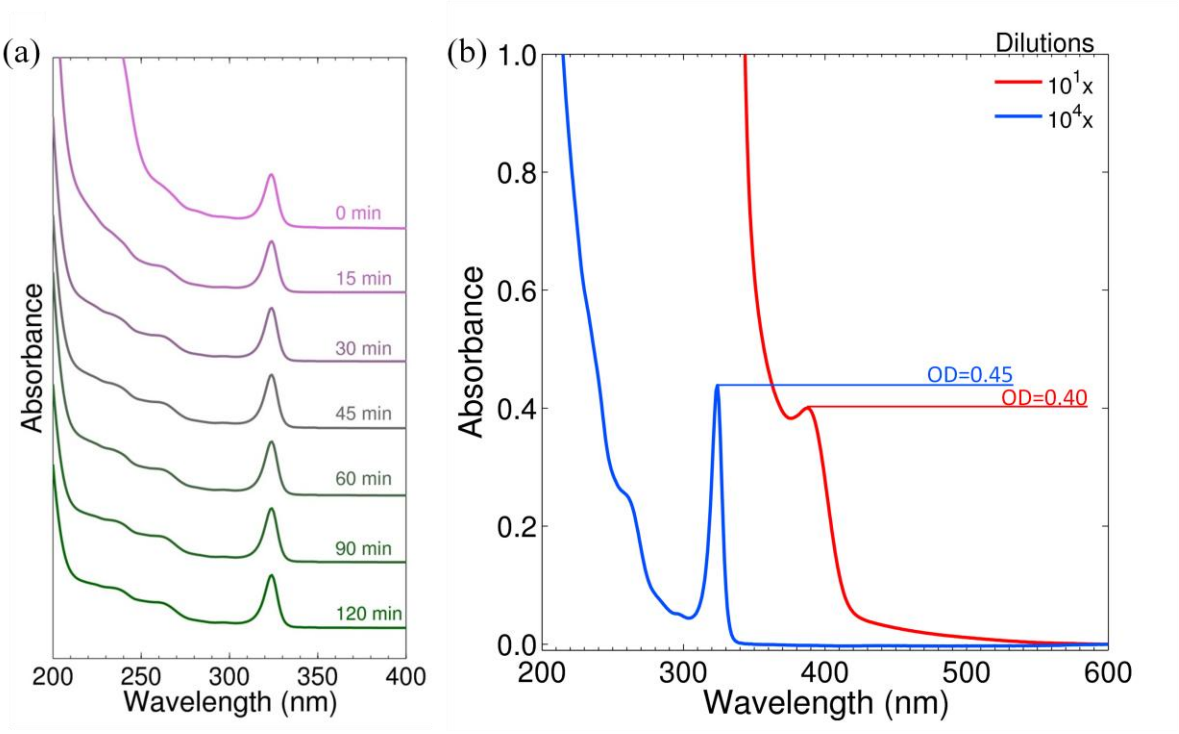

Figure 1. (a) Absorption spectra of aliquots extracted at specific times in a MSC synthesis. The spectra show the direct synthesis of the 324 nm family. As the reaction pursues, higher energy peaks are resolved due to the consumption of the precursors. (b) Dilutions of the same aliquot in the highly concentrated reaction. A dilution of 10^1x and 10^4x corresponds to the raw reactive being diluted in hexane by a factor of 10 and 10,000.

concentrated precursors are first mixed at 50°C to deter nucleation and ensure mass uniformity. The reaction mixture is heated to 147°C, at which burst nucleation of the MSC is visible and then followed with a cool to 140°C to soak. This temperature prevents continuously growing nanoparticles (CGNs) and promotes greater MSC conversion. In this particular reaction, we directly synthesize the CdS 324 nm family, which does not change over the course of the reaction (**Fig. 1a**).

When the same MSCs are synthesized under dilute conditions, we find the quality of the MSC family to be strongly dependent on how the precursors are prepared. If the precursors are made from a concentrated solution and then diluted with 1-octadecene (ODE) to a tenth of the initial concentration, the dilute reaction can synthesize the 324 nm Family. However, the reaction

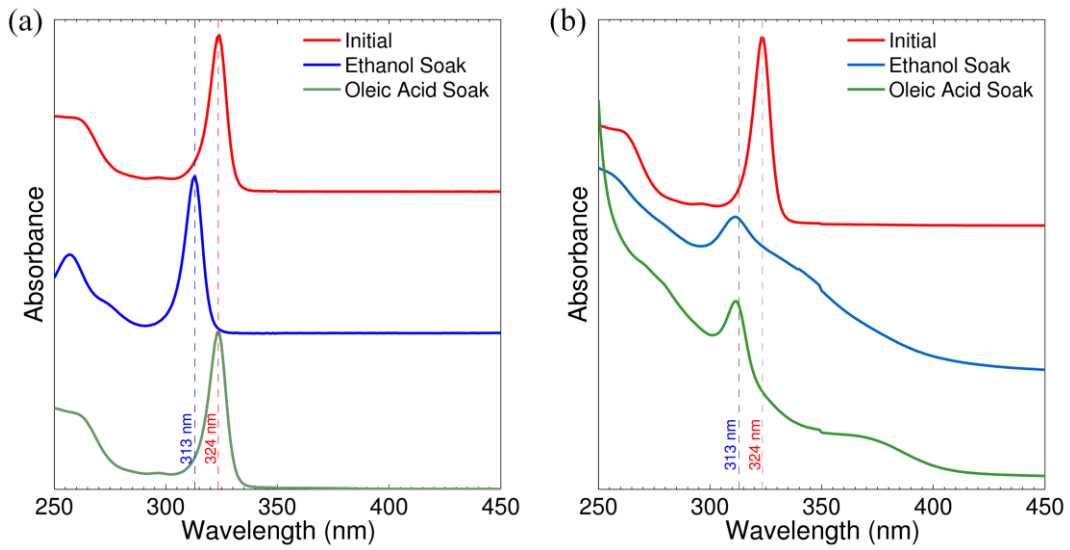

Figure 2. Absorption spectra of the MSC transformation. (a) The transformation of the 324 nm family synthesized using high concentrations. The entirety of the 324 nm family can be converted to the 313 nm family by soaking in ethanol. The 313 nm family can be reverted back by soaking in oleic acid. (b) The transformation of the 324 nm family using the dilute concentrations. To obtain a clean spectrum for the 324 nm family, the dilute product is size-selectively precipitated. When the purified product is exposed to alcohol it converts into the 313 nm family, but also produces CGNs. The reverse process does not occur in the 324 nm family produced under dilute conditions.

requires a full 60 min before any MSCs are synthesized and during this incubation period of MSC production, there is CGN formation. An incubation period of 90 min is required to observe the formation of any MSCs, if the precursors are initially prepared under dilute conditions. Consequently, the longer incubation produces even more CGNs. To test if the MSCs can be forced nucleated, we heated the reaction mixture to even higher temperature and then cooled back to 140°C. By heating the mixture to 160°C and cooling to 140°C, we find the incubation period to form MSCs can be reduced to half, but produces substantially more CGNs. When the mixture is initially heated to 180C and then cooled to 140C, there is no production of MSCs and only CGNs exist in solution. Heating to these high temperatures may change the morphology of the precursors, which will be pursued for future works. We speculate the inherent differences between the highly concentrated and dilute synthesis of MSCs are in the precursors.

To better understand the role of the precursor, we examine the cadmium to sulfur ratio of the precursors. As indicated in chapter 1, the degree to which the sulfur precursor is off stoichiometric strongly influences the stability and growth of the nanoparticle solution. A sulfur rich solution should induce large particle growth; whereas a metal rich solution remains unaltered. The average highly concentrated synthesis is performed at a Cd:S ratio of 2:1 and this yields a pure family. These is no change in the quality of the MSC or the nucleation temperature at Cd:S ratios of 4:1 and 8:1. This observation agrees with the findings in the copper sulfide synthesis. When we increase the sulfur precursor to a Cd:S ratio of 1:1 and 1:2, there is no change in the quality of the MSC. However, the nucleation temperature is lowered to 140˚C and 133˚C for the Cd:S ratios of 1:1 and 1:2, respectively. We conclude that the activation energy of the MSC is lowered at high sulfur concentrations, but there is no observable effect on the quality of the MSC under high concentrations. Currently, there is no data on the stoichiometric effects of the precursor on MSCs synthesized under dilute conditions, which will be pursued for future works.

We determine the quality of a MSC through its purity, which is determined from the optical density of its exciton to the sum of all exciton optical densities. A dilution series from the raw reaction solution is required to determine the purity of our MSCs (**Fig. 1b**). Over the course of the reaction, we maintain a consistent purity of greater than 99.9%. Using the same synthesis protocol for dilute concentrations, we synthesis the same 324 nm family, but with purities as high as 90.0%. The reduced purity of the dilute synthesis is attributed to the long incubation period required to produce the MSCs.

When the 324 nm family, synthesized by high concentrations, is washed with alcohols, the 324 nm family begins to bifurcate into the 313 nm family. If the 324 nm family is allowed to

soak in alcohols for an extended duration (~1 day at 60˚C or ~2 weeks at 25˚C) we can achieve a complete transformation of the 324 nm to the 313 nm family (**Fig. 2a**). This process is very peculiar. Traditionally, nanoparticles that are heated in anti-solvent (the alcohol) tend to promote nanoparticle growth or fragment particles[2]. More intriguing is the process can be reversed, whereby the 313 nm family is soaked in oleic acid. In literature, high concentrations of oleic acid are known to induce rampant growth of the nanoparticle, but this is not what is observed with this particular transformation[3].

To test whether this phenomena is strictly related to the MSC, we perform the same method of transformation to the MSCs synthesized under dilute condition. Given the purity of the MSCs are lower in the dilute synthesis, we have selectively precipitated the 324 nm family from the dilute product to improve the purity, such that the effects we see are only attributed to the MSC. The purified MSC is then soaked in alcohol at 60˚C for an hour. Similarly to the highly concentrated 324 nm family, we do see a distinct 313 nm. However, there is one compelling difference, in that the dilute transformation also generates CGNs (**Fig. 2b**). This is the behavior that should have been observed in the highly concentrated 324 nm family, as well. To test whether the dilute MSC can be reverted back to 324 nm, the mixed 313 nm family is soaked in oleic acid. There is no evolution of the 324 nm family and the only response is the production of CGNs. Once again, this phenomenon agrees with the reports in the literature. So, why are the MSC produced from the highly concentrated synthesis so different from that of the dilute synthesis? Additionally, we seek to answer, how do these MSC transform in a condition that would otherwise induce continuous growth of the nanocluster? Through of spectroscopy techniques we probe the entire entity that is the MSCs to identify its enigmatic structure. The organic and inorganic nature of these MSC provides insight into the latter question of the method

of transformation. In this chapter we show strong evidence of a diffusionless and reversible transformation, a coupled phenomena not yet seen in colloidal nanomaterials. We believe the approach to address the differences between the dilute and concentrated synthesis is through rheological characterization of the colloidal solution, an area of proposed research discussed in the follow chapter.

2.3 Solid-state transformation

From this point forward, we would like to define the method of transformation of the 324 nm family to the 313 nm family as the "conversion" process and the transformation of the 313 nm family to the 324 nm family as the "reversion" process. Upon exposing the MSCs to alcohols, we find the highly pure 324 nm family discretely converts into the 313 nm family. To test the nature of the transformations, thin films of the 324 nm family are made in a vapor chamber to be optically monitored by in-situ absorption spectroscopy. The films are made thin enough, such that the exciton of the MSC is less than 1.0. On average, the film thickness is between 0.5 and 2.0 microns, as to be optically transparent enough. When methanol is injected, there is an immediate bifurcation of the 324 nm family into the 313 nm family. Complete conversion of the 324 nm family is not spontaneous, but the rate of transformation can be enhanced by heating the film prior to alcohol exposure. To ensure there is no dependence on alcohol concentration, we supply enough methanol, such that the vapor is saturated and there is condensate at the bottom of the chamber. As a thin film, the MSCs are immobilized to prevent particle-particle interaction and to isolate each cluster from one another. Therefore, the only methods to induce a shift in the exciton are through cluster fragmentation or atomic restructuring. Since the method of transformation is unknown, we explore various established models that analyze the rate of transformation as if the system is in a diffusion-limited or in a kinetic-limited regime.

2.4 Magic-sized cluster fragmentation

Quantum dots are known to have tunable exctions or bandgaps, based on the size of the particle[14,15]. A shift in the exciton of a conventional dot is characteristic of a change in particle size. We observe a blue shift in our exciton, which suggests a decrease in particle size and may be attributed to particle splitting or fragmentation. If our MSCs are to split into smaller sizes, there are two observable characteristics; 1) a separate exciton for each size and 2) an increase in total particle number. Our transformation is a discrete shift to a new exciton position, indicating that our MSCs must split perfectly in half every time and then combine perfectly in the reversion. Following the idea of splitting, we should also observe a two-fold increase in particle count as the transformation finishes. However, the optical density of the fully transformed 313 nm family, which is directly proportional to a relative MSC number, is approximately the same as the initial optical density of the 324 nm family. This suggests the number of MSCs remain constant over the transformation process and the MSCs do not split. The slight offset in optical density between the pure 313 nm and 324 nm families is due to a change in extinction coefficient of the material. Using an equation that correlates photon energy to extinction coefficient, proposed by Peng, the difference in optical density can be accounted for in the conversion to particle number[14]. The other mechanism that would attribute to blue shifts in the exciton is particle fragmentation.

Prior to understand how a particle fragments, we need to identify the potential fragmenting species. The chemistry of our MSC is simple and we speculate the only species that may fragment are cadmium oleate (CdOleate) and tri-octylphosphine suflide (TOPS). Considering burst nucleation in our system is a thermally activated event, CdOleate and TOPS will be stable at the temperatures of the transformation and may exist in a free state. However,

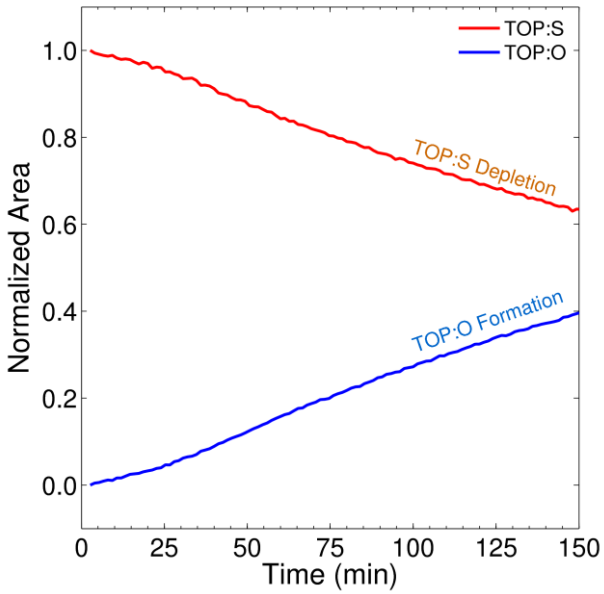

Figure 3. The change in the phosphor-31 NMR spectra as the MSCs nucleate. The area is determined by the integration of theP31- NMR peak for the P-S and P-O shifts. The area of the P-S and P-O shift is the amount of TOPS and TOPO present in the solution, respectively. The area of TOPS and TOPO are normalized by the area of the TOPS at $t = 0$. The TOPS depletes at a rate equal to the formation of TOPO.

we suggest TOPS to be an unlikely candidate for a fragmenting species. According to the in-situ synthesis of the MSCs using P31-NMR (**Fig. 3**), we find the TOPS converts directly to trioctylphosphine oxide (TOPO) at a rate very similar nucleation of the MSC. The direct formation of TOPO suggests the trioctylphosphine does not aide in the stabilization of MSC as a ligand and is unlikely to exist in the film, since the MSCs are thoroughly washed. If the MSCs are to fragment, CdOleate is the most likely candidate as the MSCs are far from stoichiometric. From ICP analysis, the cadmium to sulfur ratio is roughly 1.8 to 1.0, respectively, with an accuracy of ±1 sulfur atom. So, there is a driving force to remove cadmium atoms from the cluster. Currently, there is no conclusive evidence supporting the fragmentation of CdOleate from the MSCs to induce the electronic transformation.

Using P31-NMR on the washed MSC product prior to the transformation experiment will identify the presence of phosphines in the film. A broad peak with respect to the TOPS precursor,

at the same frequency, indicates TOPS bound to the surface of the particle. Preliminary experiments to determine whether CdOleate is an observable fragmenting species will be performed with absorption spectroscopy. To test whether CdOleate can be identified in the film, a dilution series of a known amount of CdOleate will determine the attenuation coefficient of the precursor. If the attenuating strength in the ultra-violet is near the same order as the MSCs, then any fragmentation of the CdOleate will be observable during the in-situ transformation. If the attenuating strength is significantly weaker than the MSCs, then rheological characterization is necessary. We expect a decrease in the film viscosity if the MSC fragments. This takes into consideration that CdOleate is a smaller molecular species, has a melting temperature lower than the transformation temperature, and is untethered. The melting point of CdOleate is ~50˚C and the MSCs have a higher melting temperature of ~150˚C.

2.5 Diffusion-limited transformation

To determine if the process is governed by alcohol diffusion, we fit the in-situ transformation sigmoid with diffusion-limited models. Any fluctuations from the light source or temperature can be refined out by normalizing the optical density of the 313 nm family using equation 2.1, where α defines the extent of reaction.

$$\alpha = \frac{I_{313}(t)}{I_{313}(t) + I_{324}(t)} \quad \textbf{(2.1)}$$

where I_{313} and I_{324} are the optical intensities of the absorption spectra as a function of time for 313 nm and 324 nm wavelengths, respectively. Considering the thickness of the film is much smaller than the diameter, a 1-dimensional (1-D) diffusion process is a valid assumption. Various reports of analyzing vapor diffusion into a thin polymer substrate use a semi-infinite slab assumption[4,5]. Therefore, the rate of transformation is proportional to the square root of time,

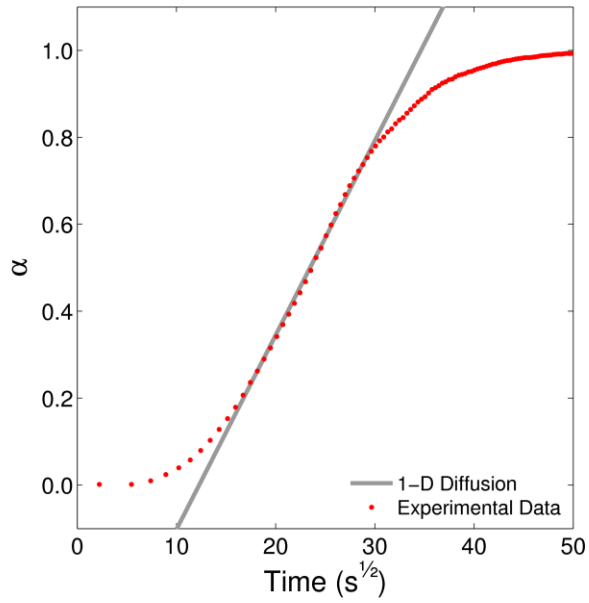

Figure 4. The evolution of the 313 nm family in term of a normalized optical intensity (proportional to concentration with the application of Beer-Lambert's Law). The experimental data is plotted with $t^{½}$ to linearize the data to extract the diffusion coefficient. Using Eq. 2, and a thickness of 1 micron, the diffusion coefficient is ~10^{-16} m^2s^{-1}.

with a diffusion coefficient proportional to the linear slope (Eq. 2.2). Although our system is a finite slab with a no flux condition at the glass substrate, we believe the semi-infinite assumption to be a good approximation at early times, as this is when most of the transformation occurs. A rate constant (k_D) of 2.0x10^{-3} s^{-1} is fitted for the slope of the linear region of the data in **Figure 4**. If the rate-limiting process is truly diffusion-limited, then a first order approximation of the diffusion coefficient can be expressed as

$$D = \frac{k_D l^2}{4\pi} \qquad \textbf{(2.2)}$$

where l is the film thickness and k_D is the rate constant. We calculate a diffusion coefficient (D) of approximately 10^{-16} m^2s^{-1}, with a film thickness of 1 micron. Given the nature of our dried MSCs have polymer-like characteristics; we compare our diffusion coefficient to those commonly seen with polymer systems. The diffusivity of gases into a polymer matrix has rates

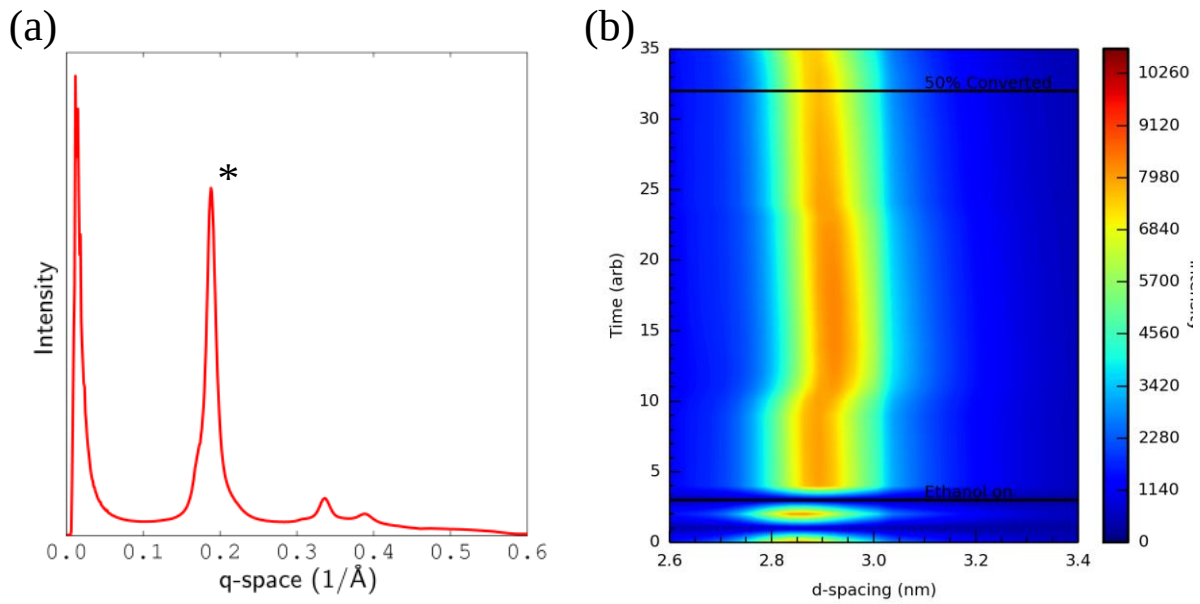

Figure 5. (a) Radial integration of the initial GI-SAXS pattern for a thin film of a 324 nm family. The peak spacing suggests the films is a hexagonally packed lamellae structure (peak spacing of 1-Q, $\sqrt{3}$-Q, and 2-Q) (b) The evolution of the 1-Q peak (highlights by *) through the transformation process. The average d-spacing of the peak is 2.90 ±0.05 nm. There is a short-lived perturbation with the introduction of the ethanol vapor. The fluctuations at long times are due to changes in the synchrontron source intensity and the source being refilled.

no slower than 10^{-10} m^2s^{-1}, which are substantially faster than the diffusivity of the MSC films[6,7]. The vast difference between diffusion coefficients, strongly suggest the transformation is not vapor diffusion-limited and that the film is fully saturated with alcohol vapor within seconds of exposure.

Although we find the vapor phase being diffusion-limited to be unlikely, we do find our diffusion rates are similar to the self-diffusivity of equal length polymer chains in a solid matrix (diffusivities of 10^{-18} to 10^{-15} m^2s^{-1})[8]. Our MSCs are passivated with oleic acid ligands, whereby the hydrocarbon tails represent a short chain polymer. Unfortunately, the self-diffusivity of the tails is a physical process, which does attribute to the transformation, as the data is representative of an electronic change. We further support this notion via in-situ grazing incidence short angle scattering (GI-SAXS), which provide insight into the spacing between MSCs. Upon radial

integration of the GI-SAXS pattern, we find the MSCs arranged in a hexagonally packed cylinder (HPC) formation (**Fig.5a**)[9]. With the introduction of the ethanol vapor, there is a small perturbation in the film. This perturbation is short-lived and is much shorter than the entire transformation process. Throughout the conversion process, the d-spacing remains fairly constant with minor fluctuations due to changes in the synchrotron source (**Fig. 5b**). The d-spacing is nearly equivalent to a fully extended oleic acid hydrocarbon tail (~2.7 nm). With these small fluctuations, the MSCs do not move the distance of an oleic acid ligand to interact with its neighboring MSC. Hence, the MSCs are non-interacting.

2.6 Kinetic-limited transformation

In the case of a kinetic-limited process, we investigate several of models to determine the type of reaction the alcohol vapor may have on the MSC film. The Avrami-Erofe'ev (A-E) model describes a power-law process whereby a "germ" nuclei is generated at a rate, *k*, (typically at a lattice defect) and is then followed by a constant radial growth rate with a growth scaling of n[10,11].

$$\alpha = 1 - \exp\left((kt)^n\right) \quad \textbf{(2.3)}$$

The value of *n* is a function of the nucleation behavior, β, and the growth dimension, δ (Eq. 2.4).

$$n = \beta + {}^{\delta}/_{2} \quad \textbf{(2.4)}$$

The value of δ is 1, 2, or 3. The nucleation behavior is between 0 and 1, where i) $\beta = 0$ defines an instantaneous generation of nuclei, ii) $0 < \beta < 1$ is deceleratory nucleation, and iii) $\beta = 1$ is constant nucleation. When we fit the A-E model to the in-situ transformation, we obtain a *k* of 1.4×10^{-3} s^{-1} and *n* of 1.5 (**Fig. 6**). We can interpret a single MSC to be equivalent to a single "germ" nucleus. The method of how the "germ" nuclei grow is characterized by the value of *n*. According to HR-STEM, we find our MSCs are confined within organic fibers that are the oleic

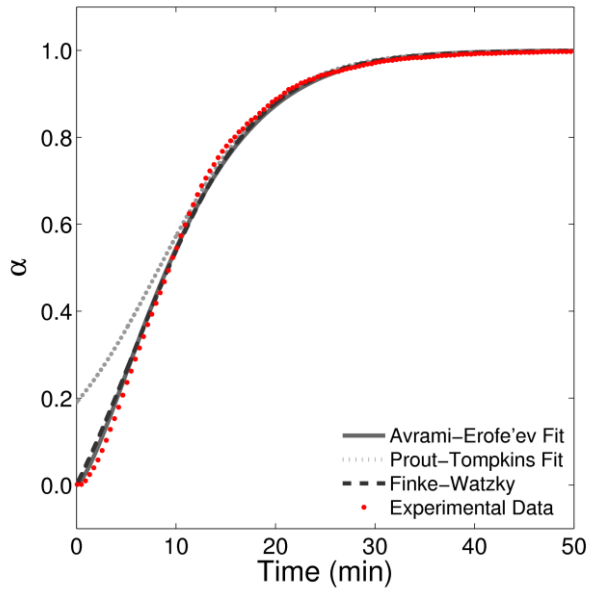

Figure 6. Experimental data of the evolution of the 313 nm family in an MSC transformation. The transformation occurs on a MSC thin film at 70˚C in the presence of methanol vapor. The data is fit with the A-E(Eq. 3), F-W (Eq. 5) and P-T (Eq.6) equations. The A-E and F-W equation fit the data with good accuracy (R^2 values of 0.999 and 0.998, respectively). The P-T equation has an R^2 of 0.965. The A-E equation is the more statistically accurate fit for this data.

acid ligands of the MSCs (**see SI**). If we assume only MSCs within a single fiber are interacting, then the dimensionality of growth is 1-Dimensional ($\delta = 1$). By factoring δ into Eq. 2.4, we obtain a constant nucleation behavior ($\beta = 1$) or a constant probability to generate a "germ" nuclei (transform the MSC), which is very likely in a film saturated with the transforming reagent (alcohol). Unfortunately, there is controversy over on the truth behind the physical interpretation of the fitting parameters in the A-E model and our physical interpretation should not be taken to be an accurate depiction of the process[12]. Additionally, the assumption of interacting MSCs is voided due to the initial system design of non-interacting MSCs.

The model that contests the A-E model is the Finke-Watzky (F-W). In the F-W model, solid-states transformations are described by auto-catalysis. There is an initiation step with rate

k_1 and auto-catalytic step with rate k_2 (Eq. 2.5)[12]. When we fit the F-W model, we obtain a k_1 of $2x10^{-3}s^{-1}$ and k_2 of $3.8x10^{-1}$ s^{-1} (**Fig. 6**).

$$\alpha = 1 - \frac{k_2 + k_1}{k_2 + k_1 \exp\left((k_2 + k_1)t\right)} \quad \textbf{(2.5)}$$

There is no physical interpretation of these fits; rather these values are just arbitrary time scales. Interestingly, the value of k_1 is the same order of magnitude as the rates from the A-E and 1-D diffusion. According to the auto-catalytic reaction, k_1 represents the nucleation rate. Similar to the F-W model in the form of the equation is the Prout-Tompkins (P-T) model (Eq. 2.6)[10,13].

$$\alpha = 1 - \frac{1}{1 + \exp\left(k_B t\right)} \quad \textbf{(2.6)}$$

The basis of the P-T model is from chain polymerization, whereby there is an initiation, propagation, and termination step. In the solid-state system, the rate constant at each step is the same. Therefore, the model is only fitted by a single parameter, the branching rate k_b. Unlike, the A-E and P-T model, a time shift of 500 s is necessary to get a moderate fit of the data. By taking the time shift into consideration, the P-T model has a k_b of $2.9x10^{-3}$ s^{-1} (**Fig. 6**). The P-T model (R^2=0.965) does not fit the data as well as the A-E and F-W (R^2=0.999 and 0.998, respectively), particularly due to the model being a single fit parameter model and poorly capture the behavior at short times.

2.7 Analysis of the MSC atomic structure

The electronic and physical structure of semi-conducting materials is highly coupled. A small shift in the atomic spacing has a significant influence on the electronic transitions in the lattice. To test hypothesize the shift in the MSC exciton is due to atomic restructuring, we perform xray total scattering on the MSCs before and after the transformation process. Analysis

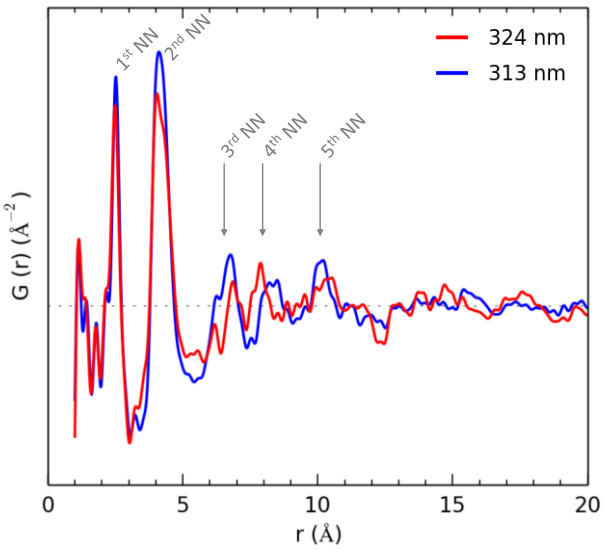

Figure 7. The reduced radial distribution function (G(r)) of the xray total scattering patterns for the 313 nm and 324 nm families. NN defines the separation between the scattering atom and its nearest neighbor. The 1st NN refers to the Cd-S bond length. The 2nd NN can be translated into the bond angles. The positions of the 1st and 2nd NN do not alter, suggesting the bond length and angle is conserved upon complete transformation. There are considerable changes in peak position for the 3rd, 4th, and 5th NN. Peak positions move as much as 1 Å.

of the total scattering provides us with information on atomic spacing and angles within the MSC structure in the form of the radial distribution (G(r)). The 1st nearest neighbor (NN) identifies the Cd-S bond distance and the 2nd NN provides information on the bonding angle of the three atoms. We find the 313 nm and 324 nm families Cd-S bond distances and angles are conserved through the transformation process. An approximate size of 1.3 – 1.5 nm is determined from the flattening of the G(r) at higher atomic spacing. The key difference between the two families is with the 3rd, 4th, and 5th NNs, which indicates a distinct difference in the structure of the two families and support the hypothesis. Given these NNs spacings are 0.7 to 1.0 nm (half the MSC size), we suggest the entire structure has reconfigured, with atoms moving up to 0.1 nm. Since the distance of the atoms have to travel is smaller than the length of the CdS bond, we propose no bonds are broken in the transformation process. Thereby, deters the transfer of mass into and out of MSC and indentifies the 313 nm and 324 nm families as structural cousins. This method

of atomic restructuring is classified as a diffusionless transformation, a phenomenon not yet observed for colloidal nanoparticle systems. We have identified the 313 nm and 324 nm families to be structural cousins that undergo a diffusionless transformation.

The challenge with G(r) is that it is a 1-Dimensional representation of a 3-Dimensional structure and there is not enough information from the experimental data to predict a structure. Therefore, known 3-Dimensional structures need to be fit to the data and the residuals of the fit determine if the structure is a good fit. This work is still in progress and techniques, such as monte carlo (MC) and genetic algorithm (GA), are being pursued. Residuals as low as 0.18 and 0.22 have been achieved for the 313 nm and 324 nm family, respectively.

2.8 Analysis of the MSC surface chemistry and structure

For oleic acid stabilized nanoparticles, the oleate functional group has a variety of different binding configurations to the surface of the nanoparticle. Through FT-IR spectroscopy we identify distinct difference in the carbonyl stretches (O-C-O vibrations) between the 324 nm family and the 313 nm family. The binding configuration is identified by the energy spacing, Δ, between the asymmetric carbonyl stretch (~1520-1560 1/cm) and the symmetric carbonyl stretch (~1400-1450 1/cm). Generally, there are two asymmetric peaks, where the lower and higher energy peak is attributed to the chelating and bridging bindentate configuration, respectively. A chelating bidentate configuration indicates one acid for each metal atom; whereas a bridging bidentate would have one acid for every two metal atoms on the surface. However, our MSCs have a singlet for the carbonyl asymmetric peak. This singlet peak is very peculiar because nanoparticles with oleic acid ligands have a mix of binding configuration. Our current hypothesis is that the surface of the 324 nm family is strictly chelating bidentate, since the MSC has a

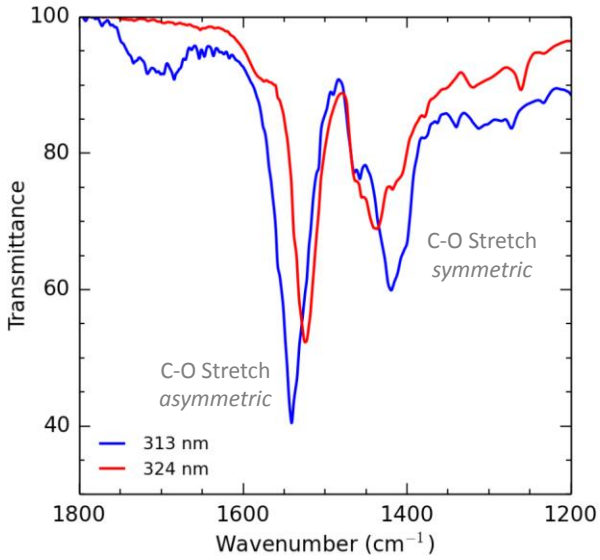

Figure 8. The FT-IR spectra of the 313 nm and 324 nm. The spectra is confined within the carbonyl (O-C-O) stretch region to analyze the oleic acid ligands. The peaks between 1525 cm^{-1} and 1550 cm^{-1} are the asymmetric carbonyl stretch and the peaks between 1420 cm^{-1} and 1440 cm^{-1} are the symmetric carbonyl stretch. The energy difference, Δ, dictates the binding configuration. Only one peak is present, so the exact determines of the binding configuration cannot be determined without a standard. We hypothesize the smaller Δ is the chelating bidentate and the larger Δ is the bridging bidentate configuration. Therefore, the oleic acid of the 324 nm family is strictly chelating and the 313 nm family is strictly bridging.

smaller Δ than the 313 nm family, which is suggested to be strictly bridging bidentate. This suggests the surface of the 313 nm and 324 nm family contains a single surface facet. Additionally, we speculate the change in ligand conformation induces the structural change in the MSC. There have been several reports of alcohols influencing how carboxylic acids are bound to the metal surfaces[2,16–19]. According to DFT calculations, the reconfiguring is due to hydrogen bonding of the acid with the alcohol or the water in the alcoho[17]. Additionally, DFT indicates that carboxylic acids configurations can be facet specific[17]. In our MSCs, if the oleic acid ligand is strongly bound to the surface, its configuration could very well dictate the surface structure of the MSC, which in turn forces a core reconstruction of the MSC.

To obtain a deeper understanding of our MSC composition, we employ XPS. When analyzing XPS, we find a noticeable shoulder in the Cd 3d spectra, which indicates a shift in its

electronic state. Traditionally, cadmium is very resilient to chemical shifts and requires highly electronegative species (Cl) to create even a small change[20]. Upon integration of the primary peak and the secondary shoulder, we find the shoulder composes of roughly 40% and 25% of the area in the 313 nm and 324 nm families, respectively. We hypothesize the observed shoulders are the surface cadmium atoms, which are strongly influenced by the ligands. Under this assumption, the 313 nm family would have nearly twice the number of cadmium atoms on the surface than the 324 nm family.

We have previously identified the 313 nm and 324 nm families to be structural cousins and hence no mass transfer into or out of the MSC. The 313 nm family is in a bridging bidentate configuration and each oleic acid is tethered to two cadmium atoms. To satisfy the bridging bidentate, there needs to be twice as many cadmium atoms on the surface than the chelating bidentate. According to the XPS analysis, the 313 nm family does have twice as many cadmium atoms on the surface than the 324 nm, necessary to satisfy the bridging bidentate oleic acid to cadmium ratio. We speculate the cadmium atoms in the core are being pulled to the surface to satisfy the more stable oleic acid bridging bidentate configuration with the presence of a hydrogen bonding species. To pull the core cadmium atoms to the surface, the MSC must decrease in size and would results in a blue shift in the exciton. With the removal of the hydrogen bonding species, the atomic structure should revert back if supplied with enough thermal energy.

2.9 Future Works

The next steps for this project are to 1) investigate if cadmium oleate is a candidate fragmenting species in the transformation process (see section 2.6), 2) perform the conversion

and reversion process at varying temperature to determine activation energies, and 3) investigate non-interacting particle models to develop a mechanism behind the transformation. Indentifying the structure and stable nature of our CdS MSCs will open the doors to the other MSC chemistries.

2.10 References

(1) Li, M.; Ouyang, J.; Ratcliffe, C. I.; Pietri, L.; Wu, X.; Leek, D. M.; Moudrakovski, I.; Lin, Q.; Yang, B.; Yu, K. *ACS Nano* **2009**, *3* (12), 3832–3838.

(2) Cass, L. C.; Malicki, M.; Weiss, E. A. *Anal. Chem.* **2013**, *85* (14), 6974–6979.

(3) Bullen, C.; Mulvaney, P. *Nano Lett.* **2004**, *4* (12), 2303–2307.

(4) Crank, J. *2nd Ed. Oxford Univ. Press. UK* **1975**.

(5) Karimi, M. *Mass Transf. Chem. Eng.* **2006**, 17–40.

(6) Wang, T.; Heermann, D. W.; Heilig, J. C. *Macromol. Theory Simulations* **2000**, *9* (9), 687–697.

(7) Metz, S. J. **2003**, *78* (8), 880–886.

(8) Yoshiyuki, F. H. E. *Polym. J.* **1985**, *17* (10), 1131–1139.

(9) Lam, C. N.; Olsen, B. D. *Soft Matter* **2013**, *9* (8), 2393.

(10) Brown, W. E.; Dollimore, D.; Galwey, A. K. *Reaction in the solid state.* ; 1980; Vol. 22.

(11) Burbelko, a. a.; Fraś, E.; Kapturkiewicz, W. *Mater. Sci. Eng. A* **2005**, *413-414*, 429–434.

(12) Finney, E. E.; Finke, R. G. *Chem. Mater.* **2009**, *21* (19), 4692–4705.

(13) Brown, M. E. *Thermochim. Acta* **1997**, *300* (1-2), 93–106.

(14) Yu, W. W.; Qu, L.; Guo, W.; Peng, X. *Chem. Mater.* **2003**, *125* (17), 2854–2860.

(15) Brown, P. R.; Kim, D.; Lunt, R. R.; Zhao, N.; Bawendi, M. G.; Grossman, J. C.; Bulovi??, V. *ACS Nano* **2014**, *8* (6), 5863–5872.

(16) Ojamäe, L.; Aulin, C.; Pedersen, H.; Käll, P. O. *J. Colloid Interface Sci.* **2006**, *296* (1), 71–78.

(17) Diebold, U. *Surf. Sci. Rep.* **2003**, *48* (5-8), 53–229.

(18) Yang, S.; Yang, B. X.; Wu, L.; Li, Y. H.; Liu, P.; Zhao, H.; Yu, Y. Y.; Gong, X. Q.; Yang, H. G. *Nat. Commun.* **2014**, *5*, 5355.

(19) Ignatchenko, A. V. *J. Phys. Chem. C* **2011**, *115* (32), 16012–16018.

(20) Lee, H. L.; Issam, A. M.; Belmahi, M.; Assouar, M. B.; Rinnert, H.; Alnot, M. *J. Nanomater.* **2009**, *2009*.

CHAPTER 3

Future Works – Preliminary results and path forward

Abstract: In this chapter, we propose various future works to test the influence of high concentrations on the nanosynthetic chemistry of the heat-up method. The governing parameter of the high concentration synthesis is the large increase in the solution viscosity. In a colloidal mixture, the non-Newtonian nature of the viscosity can be altered through the manipulation of shear rates and ion concentrations. We provide preliminary data demonstrating that nanoparticle growth is dependent on how the solution is mixed. This is especially the case for a dilute nanoparticle system. We find the leaving group ions play a significant role in the stabilization of nanoparticle growth. When these ions are removed there is a substantial drop in the solution viscosity and the nanoparticles grow at considerably faster rates. We speculate that by changing the type of leaving group, we can tune the viscosity, which in turn governs the equilibrium size of the nanoparticle. In a similar fashion, we can introduce another metal ion species. This new metal ion would not change the size of the nanoparticle, but rather the electronic properties of the material. We have demonstrated that a spike of a concentrated copper precursor does not alter the size of the nanoparticle in a highly concentrated copper sulfide synthesis. Each of the proposed works address different aspects of colloidal synthesis, but all converge to the same central question of how viscosity is coupled to nanoparticle synthesis.

3.1 The rheological impact of colloidal nanoparticle growth and colloidal structure

Motivation

The colloidal behavior of nanopaticle synthesis has vastly expanded from the early years with much of the current emphasis on the surface chemistry and surface structure[1–3]. As the understanding of nanomaterials continues to develop, so does the urge to scale-up. Previously reported in chapter 1, there have are great works on the scale-up of these materials. However, there is one aspect to colloidal synthesis that is under appreciated and ill-characterized, yet one of the most critical aspects to scale-up; this being solution mixing. There have been great strides in understanding the rheological behavior of nanoparticles in colloidal suspensions, but the nanoparticles being analyzed are prefabricated and have been removed from the mother solution[4–6]. Solution mixing does not translate linearly with scale-up, as it is a strong function on vessel geometry, solution behavior, and flow regime[7,8]. Evidently, the manner in which a solution is mixed plays a crucial role in establishing thermal and mass uniformity. As demonstrated in chapter 1, mass and thermal uniformity dictate the quality and stability of the nanoparticle reaction. We hypothesis the extreme stability of the highly concentrated reaction is through the formation of a liquid structure; whereby particle-particle interactions are ebbed, a phenomenon not apparent in the dilute reaction. Therefore, we speculate the transitions between the precursor disassociation-nucleation and nucleation-growth is due to the breakdown of the colloidal structure, promoting species interactions. These hypotheses are in line with the central question to identify the governing factor that differentiates the highly concentrated synthesis from the dilute synthesis.

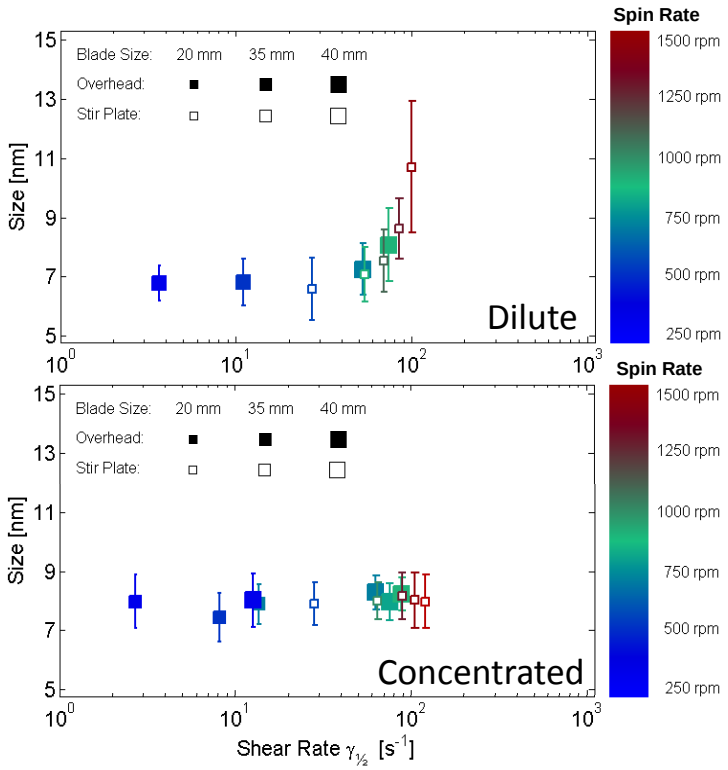

Figure 1. The effects of mixing speed and blade geometry on the growth of nanoparticle synthesis. Three different blade sizes (20 mm, 35 mm, and 40 mm) are used. Stir plate refers to a nanoparticle solution mixed by a stir bar (blade size is 20 mm). Overhead refers to nanoparticles mixed by an overhead stirrer. The color of the data points indicates the spin rate of the blade by the color map to the right of the figure. Under dilute conditions, the nanoparticle appear to be strongly influenced by mixing at high shear rates. Contrarily, the concentrated conditions have nanoparticles that are resilient to mixing. The error bars refer to the size distribution of the nanoparticles.

Impact of mixing on nanoparticle synthesis

Here, we seek to answer the effects of solution mixing or colloidal rheology on the direct synthesis of nanoparticles. To understand the effects of mixing on nanoparticle growth, we synthesis copper sulfide nanoparticle under different mixing conditions, by varying mixing speed and blade geometry. The mixing speed varies from 250 rpm to 1500 rpm. The nanoparticle solutions are mixed via a stir bar or overhead stirrer. The stir bar remains at a fixed size (20 mm), but the overhead stirrer had a variable blade size of 20 mm, 35 mm, or 40 mm. We tested the effects of mixing at two different concentrations; nanoparticles synthesized at 100 mM (dilute)

and 1000 mM (concentrated). Each reaction is prepared in the same manner, by first injecting the sulfur precursor into the copper precursor solution at 50°C with a spin rate of 400 rpm. The solution is then ramped to 185°C. Once at 185°C, we adjust the spin rate and periodically measure the rotations, to ensure the spin rate is constant throughout the experiment. Due the high speeds of some of the reaction, only the two hour end-point of the reaction is quantified via TEM, in which we determine the nanoparticle size and relative size distribution (RSD) from a Gaussian distribution fit to a 100 particles.

Preliminary evidence of changing the blade geometry and mixing speed show an influence on nanoparticle synthesis during its growth step. The focus of this study is to determine the influence of mixing rate and reaction geometry on the growth of nanoparticles. The mixing speeds of these reaction range from 250 rpm to 1500 rpm. Nanoparticles are synthesized using a stir bar (with stir plate) or overhead stirrer in various sized flasks. The size of the blade (stir bar and stirrer) and its spacing to the walls of the flask are the geometric dependence for these reactions. Given the complexity of the flow profile in a stirred vessel, we assume the shear field to follow that of a concentric cylinder (Eq. 3.1) to correlate nanoparticle size to mixing[9].

$$\gamma = NK_r \tag{3.1}$$

where N is the rotation rate and K_r is the velocity ratio to the shear rate. The expression for K_r (Eq. 3.2) is strongly dependent on the geometry of the system and the position of the fluid from the rotating blade.

$$K_r = \frac{4\pi}{n}\left(\frac{\left({R_e}/{r}\right)^n}{\left({R_e}/{R_i}\right)^n - 1}\right) \tag{3.2}$$

where r, R_i, and, R_e are the radial position of the fluid, radius of the inner cylinder (blade), and the radius of the outer cylinder (flask wall), respectively. The value of n is determined from the power-law fit to the shear dependent viscosity curves (**see SI**), which are 0.2 and 1.0 for the concentrated and dilute conditions, respectively. A "good" approximation for the average shear rate in the fluid is to use the shear rate half way between the blade and the flask wall or half-gamma ($\gamma_{½}$) expressed in Eq.. 3.3[9]

$$\gamma_{½} = \frac{\pi N 2^{2(1+{}^{1}/_{n})}}{n} \frac{\beta^{{}^{2}/_{n}}}{(1+\beta)^{{}^{2}/_{n}}(\beta^{{}^{2}/_{n}} - 1)} \quad \textbf{(3.3)}$$

where β is given by

$$\beta = {}^{R_e}/_{R_i} \quad \textbf{(3.4)}$$

The relationship between particle size and half-gamma is plotted in **Figure 1**. We find at higher mixing rates, there appears to be a trend of increasing nanoparticle size and dispersity for the dilute condition. Additionally, there appears to be a stronger mixing effect with nanoparticles mixed by a stir bar, which is the common method of mixing for nanoparticles. Current data for the highly concentrated condition does not appear to have a dependence on the mixing rate or geometry of the system.

Solution structuring of a cadmium sulfide nanosynthesis

In chapter 2, we discussed the separation of nucleation from nanoparticle growth at high concentration, potentially as a result of solution structure. To identify the structure of the solution, thin films are made by drag coating a concentrated suspension of cleaned MSCs or cadmium oleate precursor. The gap of the drag coater is set at 200 micron, but the films are thinner due evaporation or drying. These films are then mounted in front of the incident xray beam without

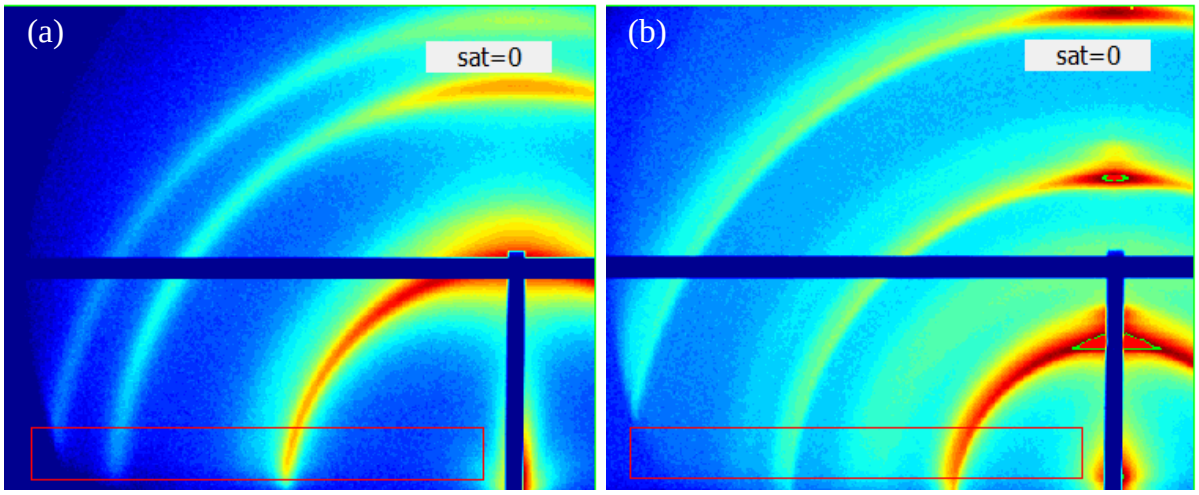

Figure 2. (a) GI-SAXS pattern of a thin film of MSCs. The pattern indicates the MSCs are in a lamellar structure with a hexagonal packed cross-section. The first ring identifies spacing between nearest neighbor MSCs in the film. The d-spacing of the MSCs are 2.9 nm. (b) GI-SAXS pattern of cadmium oleate. The pattern indicates lamellar sheets of the cadmium oleate with a d-spacing of 3.9 nm.

any further treatment. We provide preliminary evidence illustrating the existence of structure in the precursors and in the reaction at high concentrations. As the concentration lessens, the structure of the precursor fades and becomes amorphous. This phenomenon identifies a critical difference between highly concentrated and dilute reactions and addresses the central question.

We first begin analysis of the cadmium sulfide MSCs and the cadmium oleate precursor. Grazing-incidence small angle xray scattering (GI-SAXS) is used on a film of the MSCs and cadmium oleate. The scattering patterns are shown in **Figure 2**. The pattern of the MSCs indicates a lamellar material with a cross-section that is hexagonal packed cylinders (HPC)[10]; whereas the cadmium oleate is similar to that of lamellar sheets, much like the silver behenate standard. Due to safety concerns, we have not obtained a GI-SAXS pattern for the TOPS precursor, but considering the sulfur and phosphor are fairly light elements, they would scatter significantly fewer xrays than the cadmium. Although, a solid film of the material is much different than a liquid reaction, there is still a distinct difference in the innate structure. We use

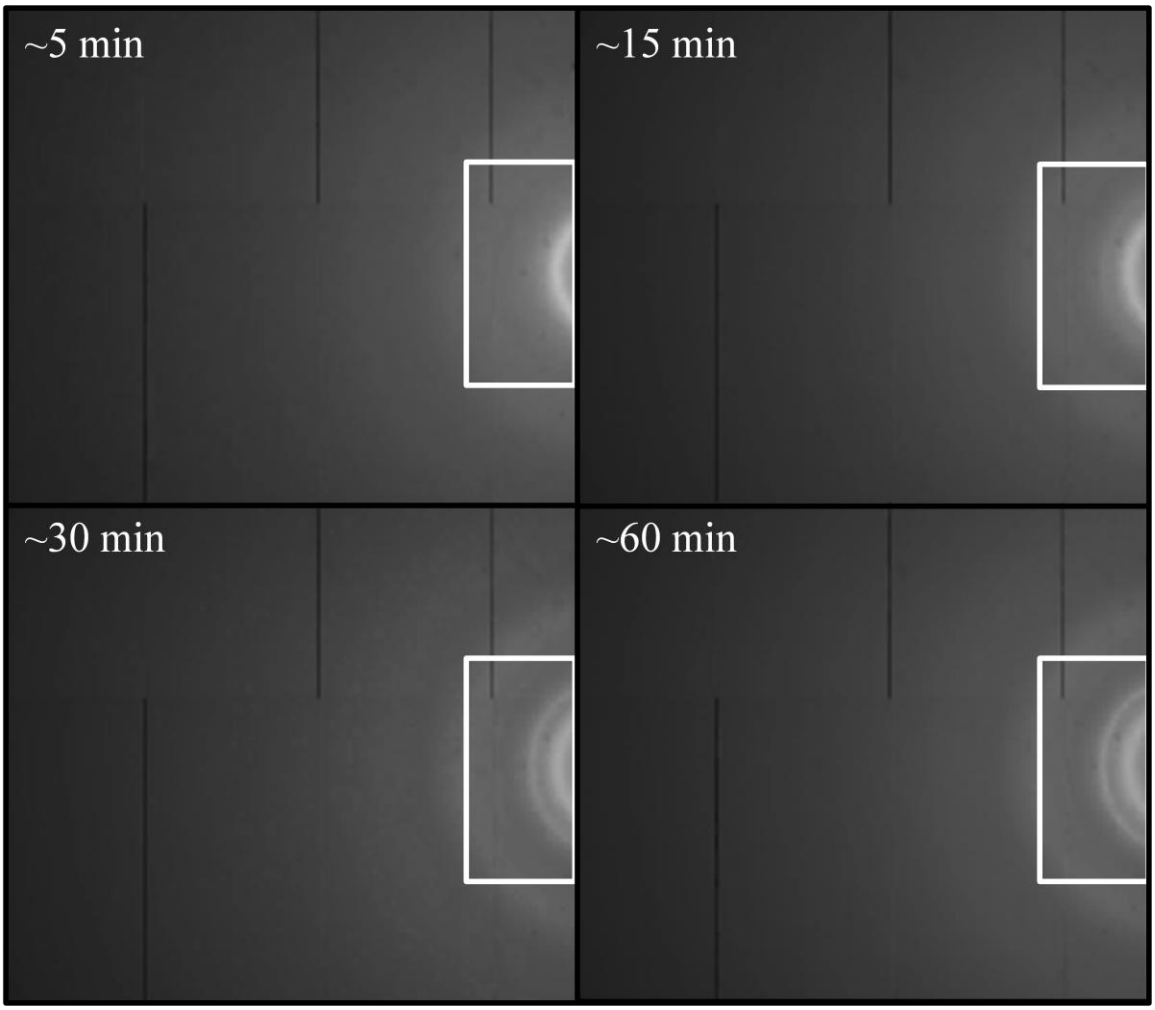

Figure 3. Snapshots of total xray scattering on an in-situ high concentrated MSC reactions. The white boxes indicate an approximate q-space the GI-SAXS pattern may represent in **Figure 2**.

these scattering patterns as endpoint references to the in-situ reaction of the MSC. The cadmium oleate characteristic of the initial precursor structure (**Fig. 2a**) and the MSC is the emerging structure (**Fig. 2b**). **Figure 3** are snapshots of a total scattering pattern of an in-situ synthesis of the MSCs at 130˚C, a temperature at which the colloidal mixture is a liquid. The white box highlights an approximation of the spectra observed in the GI-SAXS patters in **Figure 2**. Over the course of the experiment, the evolution of a new peak (d-spacing ~2.9 nm) is observed, while the precursor intensity diminishes (d-spacing ~3.9 nm).

Our next steps are to expand the in-situ xray characterization to the dilute synthesis. There several challenges associated with the dilute system that is not apparent in the concentrated reaction. The dilute system will have fewer heavy scattering atoms (cadmium), which will require either longer collection time (reduced time in-situ time resolution) or reduced signal to noise. The current xray data provides the critical insight in determining the effects of solution structure on the synthesis of nanoparticles. The follow steps for continuation of this work strictly rely on the access to Cornell's High Energy Synchrotron Source (CHESS). Given the opportunity to perform additional experiments at CHESS, we would like to 1) characterize the in-situ formation of the MSCs synthesized under dilute conditions, 2) analyze the high concentration synthesis at a much smaller q-space, 3) perform in-situ SAXS and WAXS to simultaneous identify changes in atomic structure (WAXS) with changes in solution structure (SAXS). By characterizing the solution at small angles we can compare its structure to that of the highly concentrated as a means to address the central question. Our current q-space range is between, 5 and 260 nm^{-1}. With a reduction in the q-space minimum, we can determine the MSC size and the form factor; along with achieving greater accuracy in the in-situ evolution of the MSC. Lastly, the combination in-situ SAXS and WAXS will provide additional insight into the direct formation of a single MSC family.

3.2 The influence of leaving group ions in nanoparticle growth

Traditionally, the leaving group of the metal precursor is an unappreciated component of nanoparticle synthesis as it is does not partake in the stabilization of the nanoparticle and is removed upon cleaning. A recent report by M. Hendrick *et al.*, provide a firm indication that the leaving group of a sulfur precursor strongly influences the growth rate and the equilibrium size of the nanoparticle[11]. In this section, we identify the effects of leaving group ions on the growth

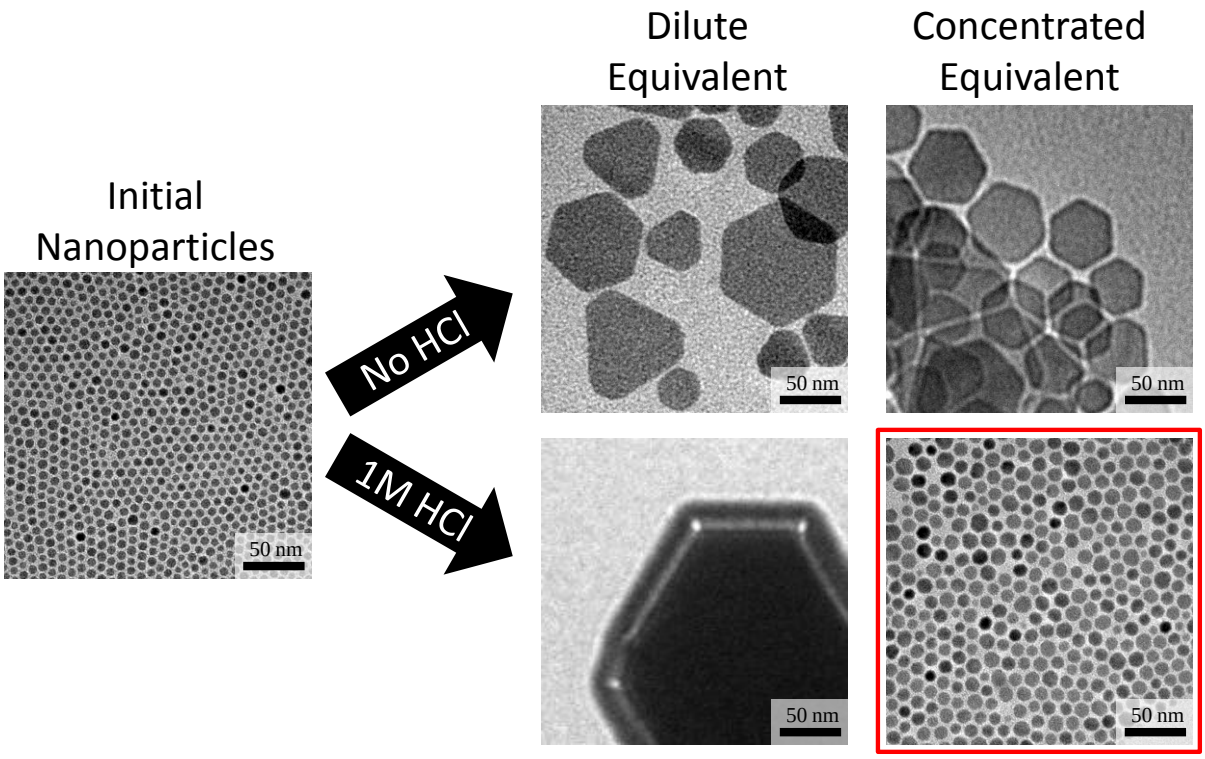

Figure 4. The effects of having the leaving group ion present during nanoparticle growth. An initial batch of copper sulfide nanoparticles are cleaned as to remove any unreacted precursor. The nanoparticle batch is suspended at dilute (0.1 g) and concentrated (1.0 g) concentrations to simulate the original synthesis concentration. Nanoparticles at dilute and high concentrations grow quickly and become large without the leaving group ion. A dilute suspension of nanoparticles with HCl grow rampantly and become bulk. A concentrated suspension of nanoparticle with HCl grow slower and still remain at the nanometer scale.

of nanoparticles and propose methods to control the growth of nanoparticles through the addition of various leaving group ions (halogens and organic conjugate bases). By analyzing involvement of the leaving group in the growth of a dilute and concentrated suspension of nanoparticles, we begin to answer the central question of how the concentrated synthesis of nanoparticles differs from that of the dilute concentrations.

To test how critical the leaving group is in the synthesis, a single batch of copper sulfide nanoparticles are precipitated using a modified synthesis method presented in chapter 1. The concentrated sulfur precursor is first injected into the copper solution at 50°C and heated to 185°C. Rather than the nanoparticles soaking for 2 hours at the top of the ramp, we precipitate

the particles as soon as the temperature of the synthesis reaches the soaking temperature. A single batch of nanoparticles is used for the analysis of the leaving group ion to ensure consistency between the results. The cleaned nanoparticles are then suspended back into solution with an equivalent concentration to the original solution (0.1 g of nanoparticles for the dilute and 1.0 g of nanoparticles for the concentrated). The suspension then soaks for 2 hours, after which the nanoparticles are precipitated and analyzed through TEM (**Fig. 4**). The suspending solution is pure oleylamine (OLA) or OLA with the addition of 1 mL of 10.0 M HCl to make a 1 M solution of HCl in OLA. The 1 M HCl provides chlorine ions at a concentration equivalent to chlorine leaving group concentration of the original reaction.

Preliminary data of the effects of removing the leaving group can be seen in the micrographs of **Figure 4**. Without the addition of HCl, both the dilute and concentrated suspension of nanoparticles has growth rates similar to that of a dilute 100 mM synthesis. Now, when the nanoparticles are in a dilute suspension in the presence of HCl, we find the growth becomes rampant and the nanoparticles quickly go to bulk and precipitate out. This behavior is to be expected, especially considering there is a high concentration of a strong acid in the nanoparticle suspension. Strikingly though, when the particles are in a concentrated suspension with the same amount of HCl, we find the growth is slowed and the nanoparticles are still nanoparticles. This goes back to the question in the chapter 2, why are the MSC produced from the highly concentrated synthesis so different from that of the dilute synthesis? The approach to this answer is through the solution viscosity. By visually comparing the flow behavior of the colloidal suspension, we see that the dilute and concentrated suspension in pure OLA to be very fluid at low and high temperatures. We see the same observation for the dilute suspension with 1

M HCl present. However, the concentrated suspension with HCl is considerably more viscous than the previous conditions.

Given the preliminary data, we propose the following next steps: 1) measure the viscosity of varying leaving group ion concentration at both suspension concentrations, 2) vary the leaving group chemistry using the conjugate based of the halogenated and organic acids, and 3) develop a model coupling leaving group ion strength to the equilibrium nanoparticle size. Quantifying the viscosity of the suspension will help describe the diffusive behavior of the nanoparticles, which we can link to the growth rates. In colloidal suspensions, the ion concentration can strongly dictate the viscosity of the solution and promote stabilization of the particle via electron screening[12,13]. By changing the leaving group ion post dissolution of the precursor, we believe we can tune the equilibrium size of the nanoparticle, similar to the works of Hendricks[11]. We will determine if there is a correlation between the leaving group and the solution viscosity. The correlation will address the central questions by identifying if the difference between the dilute and concentrated synthesis is due to the leaving group ion.

3.3 Adapting high concentration synthesis to new nanoparticle chemistries

Motivation

The novelty of high concentration synthesis of nanoparticles lies within the enhanced control of reaction and physical rates. With the separation of the nucleation and growth more challenging nanoparticle systems can be explored. In particular, the ternary and quaternary metal sulfides nanomaterials have been gaining momentum as "non-toxic" alternatives to visible light fluorescing quantum dots (QDs)[14–16]. The most promising being the doped $CuIn(M_2,M_3)S_2$ (CIS), where M_2 is a divalent and M_3 is a trivalent transition metals[17]. One of the most apparent

challenges with the CIS system is the nanoparticle emission is achieving a narrow emission spectrum. Generally, the emissions of these materials are very broad with low quantum yields. In most cases, the low quantum yields are a result of large polydispersity and crystalline defects in the nanoparticles.

We believe the challenges of high polydispersity can be addressed using the high concentrations methods to isolate nucleation step. The isolation of nucleation step enables us to introduce dopants early into the colloidal matrix and ensure the dopants are uniformly distributed, such that the nanoparticles experience the same growth trajectory. Ultimately, this proposed work will seek to further answer the central question, how does the nanosynthetic chemistry of the heat-up method differ when concentrations are intensified? And more specifically, we seek to answer, the effects of dopants in the copper sulfide nanoparticle lattice?

Nanoparticle Chemistry and Method

In this work, we will synthesize $CuGaS_2$ and $CuFe(Sn)S_2$ expanding upon the same highly concentrated method described in chapter 1. The benefit of the high concentration synthesis is its resilience towards system perturbations. We have shown the highly concentrated system is quick to equilibrate after being spike with a copper precursor. By changing the copper precursor to another metal salt, we believe we can dope the copper sulfide without changing the quality or size of the nanoparticle. With the same size particle, we can directly analyze the effect of doping on the copper sulfide nanoparticle system. An alternative approach to analyze the effects of doping will be the incorporation of the doping species prior to the nucleation phase of the material. We can identify the relative reactivity of the doping species to the copper precursor by varying the concentration and chemistry (e.g. halides, organic conjugate bases) of the leaving

group. In turn, these leaving groups will affect the viscosity and colloidal stability. We will connect these findings with the future work proposed in section 3.2, to see if there is a correlation between reactivities of doping metals and leaving group ions.

There is little fundamental understanding of how the nanoparticles are doped; especially when considering the nanoparticles have a tendency to purge impurities from the crystal. The current understanding is through the idea of Pearson's Hard-Soft Acid-Bases (HSAB), whereby soft acids and bases are more tightly bound to one another, likewise for the hard acids and bases[21]. Therefore, balancing the level of dopants and leaving groups is critical for a stable particle, a concept incited by the previous section. For the CIS system, copper is a soft Lewis acid and indium is a hard Lewis acid, which results in different reactivity of the two metals and a potential to phase segregate[22]. The inconspicuous truth to the CIS material system as a material for commercialization, hence scale-up, is the limited natural abundance of the indium element. Instead, we will explore the doped copper sulfide systems using gallium and iron (trivalent metals). $CuGaS_2$ and $CuFe(Sn)S_2$ are both semiconducting nanomaterials with tunable optical bandgaps as a function of doping concentration and nanoparticle size[14,18–20].

The most common approach to ternary and quaternary materials is to have all metal species present prior to particle nucleation. Given the discrepancies between the reaction rates, this may be the issue leading to broad emissions; whereby each particle becomes a different size and composition. With our high concentration synthesis, we can take two approaches; 1) have both metal species present during nucleation or 2) introduce the second metal species after generation of the copper seeds (nuclei). At high concentrations, we can tune the reaction rates of the two species, such that the rates become equivalent to produce seeds of the desired composition. We can control the rates through the viscosity and the leaving group, as alluded to

previously in this chapter. Being capable of controlling the solution viscosity is a control parameter the typical dilute syntheses are unable to modify without drastic changes to the colloidal mixture. Additionally, the isolation of the nucleation step is challenging for the typical synthesis and requires quenching. Hence, we can keep the same colloidal mixture the seeds, where they are stable, and introduce the new species to dope with. The introduced species will be in high concentrations and generate a large driving force of the species between the liquid solution and the initial seed. In chapter 1, we have shown the highly concentrated reaction does respond to copper precursor spike and the system is capable of restoring to a uniform size distribution. With this notion, we can change the precursor to another metal salt and spike the highly concentrated reaction during the growth phase of the synthesis.

3.4 References

(1) Owen, J. S.; Park, J.; Trudeau, P. E.; Alivisatos, a. P. *J. Am. Chem. Soc.* **2008**, *130* (37), 12279–12281.

(2) Anderson, N. C.; Hendricks, M. P.; Choi, J. J.; Owen, J. S. *J. Am. Chem. Soc.* **2013**, *135* (49), 18536–18548.

(3) Cass, L. C.; Malicki, M.; Weiss, E. A. *Anal. Chem.* **2013**, *85* (14), 6974–6979.

(4) Rudyak, V. Y.; Krasnolutskii, S. L. *Phys. Lett. Sect. A Gen. At. Solid State Phys.* **2014**, *378* (26-27), 1845–1849.

(5) Rudyak, V. Y. *Adv. Nanoparticles* **2013**, *2* (August), 266–279.

(6) Verberg, R.; de Schepper, I. M.; Cohen, E. G. D. *Phys. Rev. E* **1997**, *55* (3), 3143–3158.

(7) Shervin, C. R.; Raughley, D. A.; Romaszewski, R. A. *Chem. Eng. Sci.* **1991**, *46* (11), 2867–2873.

(8) R.P. Chhabra, J. F. R. *Non-Newtonian Flow and Applied Rheology*; 2008; Vol. 02.

(9) Bousmina, M.; Ait-Kadi, a.; Faisant, J. B. *J. Rheol. (N. Y. N. Y).* **1999**, *43* (2), 415.

(10) Lam, C. N.; Olsen, B. D. *Soft Matter* **2013**, *9* (8), 2393.

(11) Hendricks, M. P.; Campos, M. P.; Cleveland, G. T.; Plante, I. J.; Owen, J. S. *Science (80-.).* **2015**, *348* (6240), 1226–1230.

(12) Ogawa, A.; Yamada, H.; Matsuda, S.; Okajima, K.; Doi, M. *J. Rheol. (N. Y. N. Y).* **1997**, *41*, 769.

(13) Rudyak, V. Y.; Krasnolutskii, S. L.; Ivanov, D. a. *Dokl. Phys.* **2012**, *57* (1), 33–35.

(14) Jo, D.-Y.; Kim, D.; Kim, J.-H.; Chae, H.; Seo, H. J.; Do, Y. R.; Yang, H. *ACS Appl. Mater. Interfaces* **2016**, 6–12.

(15) Shen, P.-C.; Lin, M.-S.; Lin, C.-F. *Sci. Rep.* **2014**, *4*, 5307.

(16) Kolny-Olesiak, J. *CrystEngComm* **2014**, *16* (40), 9381–9390.

(17) Perera, S. D.; Zhang, H.; Ding, X.; Nelson, A.; Robinson, R. D. *J. Mater. Chem. C* **2015**, *3* (5), 1044–1055.

(18) Liang, D.; Ma, R.; Jiao, S.; Pang, G.; Feng, S. *Nanoscale* **2012**, *4*, 6265.

(19) Khadka, D. B.; Kim, J. *J. Phys. Chem. C* **2014**, *2*, 140619070724000.

(20) MacHani, T.; Rossi, D. P.; Golden, B. J.; Jones, E. C.; Lotfipour, M.; Plass, K. E. *Chem. Mater.* **2011**, *23* (24), 5491–5495.

(21) Xie, B.-B.; Hu, B.-B.; Jiang, L.-F.; Li, G.; Du, Z.-L. *Nanoscale Res. Lett.* **2015**, *10* (1), 86.

(22) Xie, R.; Rutherford, M.; Peng, X. **2009**, No. 12, 5691–5697.

APPENDIX

The following pages are related supporting information

Supporting Information

The prodigious effects of concentration intensification on nanoparticle synthesis: a high-quality, scalable approach

Curtis B. Williamson[‡§], Douglas R. Nevers[‡§], Tobias Hanrath[‡]*, Richard D. Robinson[†]*

[‡]School of Chemical and Biomolecular Engineering, Cornell University, Ithaca, New York 14853, United States, [†] Department of Materials Science and Engineering, Cornell University, Ithaca, New York 14853, United States.

*Corresponding authors: th358@cornell.edu and rdr82@cornell.edu.

[§] These authors contributed equally to this work.

Experimental Methods

Materials

The following chemicals were used as received: oleylamine (OLA, 98% primary amines), 1-octadecene (ODE, 90%), oleic acid (OA, 90%), copper(I) chloride (97%), cadmium oxide (99.5%), lead (II) oxide (99.0%), and elemental sulfur (purified by sublimation, particle size~100 mesh) were purchased from Sigma-Aldrich. Hexanes (BDH ACS Grade) and ethanol (Ethanol, 200 proof, Anhydrous KOPTEC USP) were purchased from VMR International. Tri-n-octylphsosphine (TOP, 97%) was purchased from Strem Chemicals.

Synthesis of $Cu_{2-x}S$ Nanoparticles

Sulfur oleylamine (S:OLA) was reacted with dissolved CuCl (2:1 molar ratio) to synthesize $Cu_{2-x}S$ nanocrystal. In a three-necked flask with a condenser and stir bar, CuCl was mixed with solvent (70%/30% oleylamine/1-octadecene) (OLA/ODE) to a specific concentration (0.1-1.0 M). Specific reactions quantities are provide in **Table S1.** The solution was degassed under vacuum and heated to and held at 110°C for 1 hr to dissolve, and then cooled to 50˚C and placed under nitrogen. The solution was considered dissolved when it had turned a transparent tan or copper color, which was darker for higher concentrations. For the sulfur, in a three-necked flask with a condenser and stir bar, a specified concentration of sulfur (0.5-5 M) was prepared in solvent (70%/30% oleylamine/1-octadecene). The sulfur concentration was always 5 times that of the copper solution. The sulfur solution was degassed at room temperature and then place under N_2 and heated to 110 °C for 1 hr to dissolve the sulfur. As the yellow sulfur particulates dissolved, the solution turned dark red and no particulate were visible. The solution was considered dissolved when the solution is a uniform dark red color. The sulfur solution is then cooled to room temperature. The viscosity of both solutions substantially rises as they cool, but do not solidify. If the copper solution is cooled too quickly (forced convection), it will solidify.

At 50˚C, 1 mL of the S:OLA solution was injected into the copper solution, and the solution immediately turned black. The reaction was heated following a specified time-temperature profile and then quenched in cool water. During the quench, when the reaction reaches 100˚C, the reaction is injected with equal parts (to the reaction volume) of hexane or ethanol to further enhance cooling and prevent solidification of reaction media. The $Cu_{2-x}S$ NPs were purified by precipitating in ethanol, centrifuging (7 min at 4400 rpm) and redispersed in hexane via sonication. This purification process was repeated again before TEM, and a third time before XRD, samples were prepared. The typical temperature profile was a 5 min hold at 50˚C after injection to mix, then ramped to 185˚C at a rate of 6.75°C/min (20 min ramp). Upon reaching 185°C, the reaction solution was maintained at 185°C for 1-4 hours.

Table S1: $Cu_{2-x}S$ NPs specific reaction quantities.

Copper Precursor				Sulfur Precursor			
Copper Concentration (mM)	**CuCl Mass (g)**	**OLA Volume (mL)**	**ODE Volume (mL)**	**Sulfur Concentration (mM)**	**S Mass* (g)**	**OLA Volume (mL)**	**ODE Volume (mL)**
100	0.1	7	3	500	0.16	7	3
300	0.3	7	3	1500	0.48	7	3
500	0.5	7	3	2500	0.80	7	3
750	0.75	7	3	3750	1.20	7	3
1000	1	7	3	5000	1.60	7	3

*Only 1 mL was injected into the copper precursor

Synthesis of CdS nanoparticles

Tri-octylphospine sulfide (TOPS) was reacted with CdOleate (1:1 molar ratio) to synthesize *CdS* nanoparticles. In a three-necked flask with a condenser and stir bar, 10 mmol of CdO was mixed in 10 mL of oleic acid (OA) and degassed under vacuum. The mixture bubbles vigorously and becomes frothy. While maintaining froth level, the mixture is heated to and held at 110˚C for 30 min, while still under vacuum. During this time, the mixture becomes transparent and the bubbling subsides. The solution is further heated to 160˚C and remains at 160˚C until the additional bubbling subsides, after which the solution is cooled to 50˚C and placed under N_2. During cooling, the viscosity of the solution substantially rises and becomes a gel at 50˚C. In a N_2 glovebox, a 2.5 M TOPS solution was prepared by dissolving 0.4 g (12.5 mmol) of elemental sulfur in 5 mL (4.16 g) of TOP at room temperature in a 20 mL disposable glass vial. The solution was considered dissolved when there are no residual sulfur particulates.

The TOPS solution is removed from the glovebox and placed inside the fumehood. Via a syringe, 4 mL of the TOPS solution is extracted from vial and injected into the 50˚C CdOleate solution. The same heating profile, quenching, and cleaning procedures as the *$Cu_{2-x}S$ synthesis* were used.

Synthesis of PbS nanoparticles

S:OLA was reacted with PbOleate (1:1 molar ratio) to synthesize *PbS* nanoparticles. In a three-necked flask with a condenser and stir bar, 10 mmol of PbO was mixed in10 mL of oleic acid (OA) and degassed under vacuum. The mixture bubbles vigorously and becomes frothy. While maintaining froth level, the mixture is heated to and held at 110˚C for 30 min, while still under vacuum. During this time, the mixture becomes transparent and the bubbling subsides. The solution is further heated to 160˚C and remains at 160˚C until the additional bubbling subsides, after which the solution is cooled to 50˚C and placed under N_2. During cooling, the viscosity of the solution substantially rises and becomes a gel at 50˚C. Similar to the *$Cu_{2-x}S$* nanoparticles, a 5.0 M S:OLA solution was prepared by dissolving 0.8 g (25 mmol) of elemental sulfur in 5 mL of OLA/ODE mixture. The solution was degassed at room temperature and then place under N_2 and heated to 110 °C for 1 hr to dissolve the sulfur. The solution was

considered dissolved when the solution is a uniform dark red color. The sulfur solution is then cooled to room temperature.

2 mL of the S:OLA was injected into the PbOleate solution at 50˚C. The solution was initially two phase, but becomes a homogenous black color over the 5 min of mixing at 50˚C. The same heating profile, quenching, and cleaning procedures as the *$Cu_{2-x}S$ synthesis* were used.

Characterization Techniques

Transmission electron microscopy (TEM) analysis was performed on an FEI Tecnai T12 transmission electron microscope operating at 120 kV with a LaB_6 tip. Samples for TEM analysis were prepared by placing a drop of NP solution in hexane on top of a copper grid coated with an amorphous carbon film. Particle counting was done manually using ImageJ (0.33 nm/pixel resolution). A 100 nanoparticle count was used to measure average size and relative size distribution.

X-ray powder diffraction (XRD) data were collected on a Scintag Theta-Theta X-ray diffractometer (Cu Kα radiation, ~ 1.54 Å). Samples were washed with ethanol, centrifuged, and resuspend in hexane three times. After the three wash, the samples were dried overnight before XRD analysis.

Viscosity measurements were performed on an Anton Paar Physica MCR 501 rheometer using a 5-cm parallel plate and gap of 0.05 mm. For viscosity measurements, raw samples were extracted from the reaction at 50°C, and cooled to room temperature before being placed in the rheometer. The samples were sheared at 10 s^{-1} while heating from 25°C to 185°C at 5°C/min**.** Above 120 °C vapor loss begins to be significant impairing the reliability of the data.

Dynamic light scattering (DLS) were performed on Zetasizer Nano-ZS (Malvern Instruments Inc), and a Dip Cell (ZEN1002) was used for zeta-potential measurement. Huckel theory was used to evaluate the zeta-potential. Sample solutions were prepared similar to those used for TEM analysis. The purified solution was diluted in hexane to the order of 1-10 mg/mL, which provide a colored transparent solution for analysis. A 2 min equilibration time was used for each measurement and three replicates were taken.

Heat capacity measurements were completed on DSC Q2000 (TA Instruments Inc.). Samples were prepared in similar method as for viscosity measurements. The samples were cooled initial to -180˚C before a run started. Then, heated from 0 to 185 °C of 5-10 °C/min. The sample loses mass during the run, so value above 120 °C (similar to viscosity measurements) should not be considered reliable.

Thermogravimetric analysis was performed on EXSTAR SII TG/DTA 6200 (Seiko Instruments Inc.) or TGA Q500 (TA Instruments Inc.). Samples were prepared similar to those for XRD. The following temperature profile was used 10°C/min ramp from 25°C to 600°C, and hold at 600°C for ~10 min.

UV-Vis-NIR absorption measurements were performed on Cary 5000 UV-Vis-NIR (Aligent Technologies). Samples were suspended in hexane or TCE.

Photoluminescence (PL) measurements were performed on Horiba Fluoromax 4. Samples were suspended in hexane or TCE with an excitation source of 350 nm and a slit of 3 nm.

Supplemental Data and Analysis

Survey of Conventional Concentrations for NP Synthesis

Table S2: Survey of Conventional Concentrations for NP Synthesis with specific precursors and solvents. Notably, metal concentrations are typically ≤100 mM, and 400-1000 mM chalcogen.

Chemistry	Metal Precursors	Chalcogen Precursors	Solvent	Metal Conc.(mM)	Chalcogen Conc. (mM)	Ref
CdSe	Cadmium myristate	Se	ODE	16	8	[1]
Cu2S	Cu(acac)2	S	Oleylamine	20	10	[2]
CdS	Cd(tetradecanoate)	N-n-hexyl-N',N'-di-n-butylthiourea	hexadecane/ diphenylether	25	400	[3]
ZnS	Zn(OA)2	thiourea	octadecene/tetraglyme	32	400	[3]
CdSe	Cd(OA)2	Se	OLA/ODE,TOP	40	1020	[4]
Cu2S	Cu(acac)2	S	Oleylamine	50	25	[5]
Cu2S	Cu(acac)2	thiourea	ODE/OLA/diphenyl ether	84	1000	[3]
PbS	Pb(OA)2	N-dodecyl-N'-phenylthiourea	octane	155	3052	[3]
CdS	CdCl2	S	OLA	100	150	[6]
CdS	CdCl2	S	OLA	100	1200	[6]
ZnS	ZnCl2	S	OLA/TOPO (10mL,2.3g)	159	2400	[6]
PbS	PbCl2	S	OLA	200	332	[6]
MnS	MnCl2	S	OLA	200	400	[6]

Table S3: Thermal and physical properties of NP solutions and the mixed suspending solvents[a]

	Melting Point (°C)	Volumetric Heat Capacity ($J/m^3 \bullet °C$) at 50°C[a]	Thermal Diffusivity[b] (m^2/s) at 50°C	Shear Viscosity (mPa·s) at 120°C	Mass Diffusivity[c] (m^2/s) at 120°C
1000 mM	~40	$3.7 \cdot 10^6$	$4.0 \cdot 10^{-8}$	3.8	$2.8 \cdot 10^{-11}$
500 mM	-	-	-	2.5	$2.1 \cdot 10^{-11}$
100 mM	~30	$2.2 \cdot 10^6$	$5.7 \cdot 10^{-8}$	0.81	$13.0 \cdot 10^{-11}$
70%/30% OLA/ODE	14-16 ODE[d] 18-26 OLA[d]	$1.3 \cdot 10^6$	$11.4 \cdot 10^{-8}$	0.77	$33.0 \cdot 10^{-11}$ [e]

[a] See **Figure S15** for measurement details, and value was converted to volumetric value using mass-averaged density (solvent=0.813 g/cm^3; $Cu_{2-x}S$=5.6 g/cm^3; 100 mM has 1 wt% fraction and 1000 mM has 10 wt% based on theoretical yield), [b] Thermal diffusivity calculated based on specific heat capacity, mass-averaged density, and an approximate thermal conductivity value (0.13 W/m) (for reference, values for salts and engine oil are ~0.25 and ~0.13 W/(m K), respectively[7–9]), [c] Calculated from Stokes-Einstein assuming particle size of 5.5 nm, [d] Literature values from Sigma-Aldrich, [e] Calculated from

Stokes-Einstein, assuming a particle size corresponding to oleylamine's length (2.3 nm). This value is on the same order as self-diffusivity determined from a previously published NMR study[10].

Table S4: Comparison of solution conditions between conventional (100 mM) and highly concentrated (1000 mM) solutions

Concentration	Yield (%)	Particle Concentration (NP/L)	Unreacted precursor Concentration (mM)	Inter-particle spacing (nm)[a]	NP Diameters between particles[b]	Smoluchowski Collision Frequency[11] or Rate[d] (NP/s)	Relative Collision Rate (1/s)
100 mM	82	10^{19}	8.5	58	5.5	1.37×10^{5}	1.37×10^{-14}
1000 mM	88	10^{20}	53	27	2.5	2.5×10^{5}	2.5×10^{-15}
Superlattice[c]	-	10^{21}	-	10.6	~1	-	-

[a]Including ligands (6 nm NP core; 2.3 oleylamine ligand =10.6 nm NP). Mean interparticle spacing calculated from r=(3/(4*π*n))^(1/3) where r is the mean interparticle distance and n is the number of particles per volume. [b]Inter-particle spacing divided by the 10.6 nm NP diameter with ligands. [c]For FCC close-pack, particle concentration is determined as 4 NP/unit cell, and the unit cell length is $a = \frac{2d}{\sqrt{2}}$. [d]Collision frequency is based on a Smoluchowski collision equation (see sample calculations for additional details).

Table S5: Comparison of R^2 values for the fitted supporting **Figures S17, S18, and S19**

Concentration	Figure S14[a] Huang model[12]	Figure S15[b] KJMA model[13]	Figure S16[c] Finney model[14]
100 mM	0.963	0.979	0.990
300 mM	0.951	0.965	0.981
500 mM	0.964	0.998	0.943
750 mM	0.886	0.969	0.843
1000 mM	0.977	0.989	0.987

[a]R^2 values for each concentration to the model proposed by Huang *et al*[12]. [b]R^2 values for each concentration to the KJMA model[13,15]. [c]R^2 values for each concentration to the model proposed by Finney *et al*[14,15].

Comprehensive TEM analysis of NP size distribution

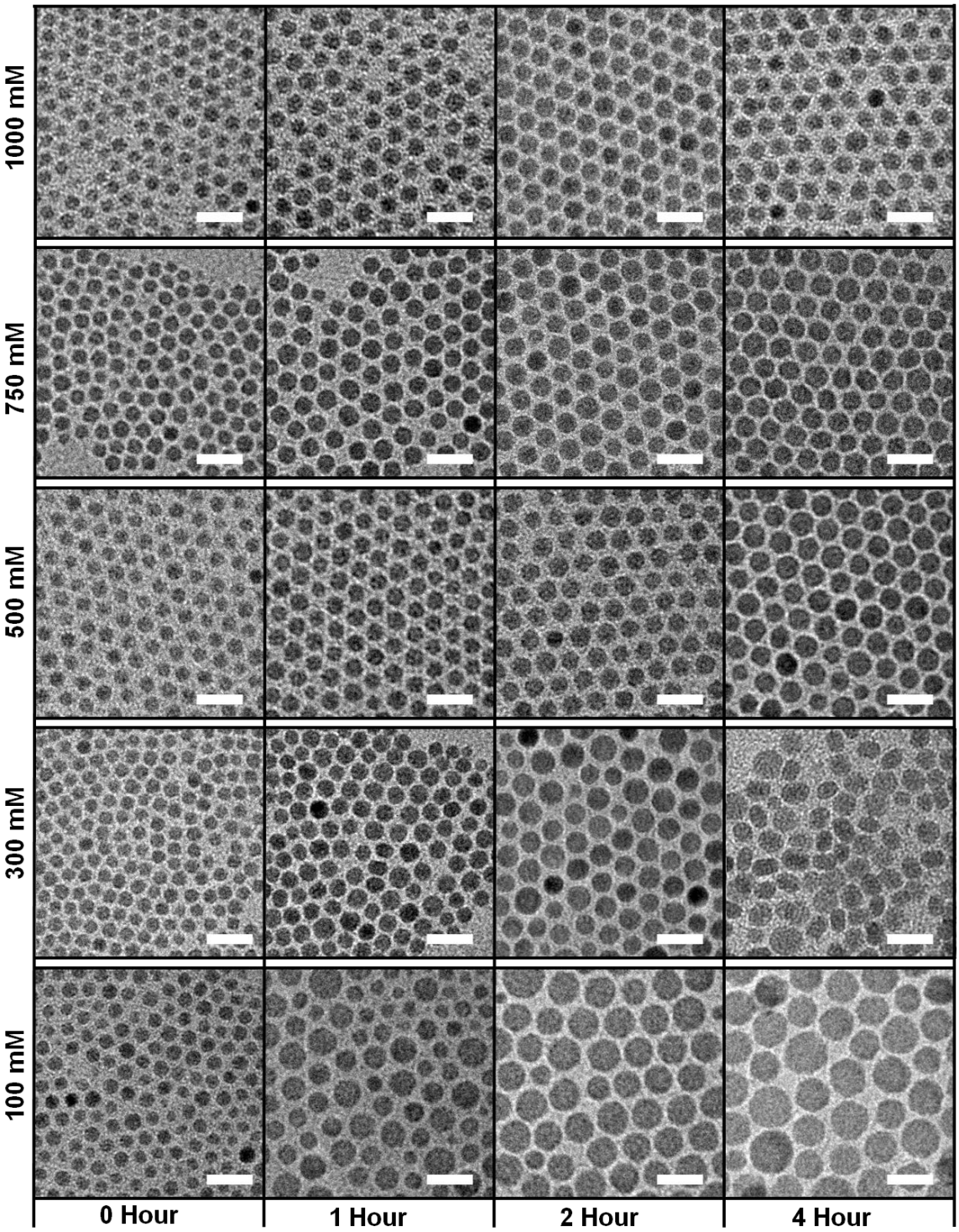

Figure S1. A series of TEMs and their size distribution (100 NP count) for several soak times (columns) and concentrations (rows). TEMs correspond to data in **Figure 3**. TEM scale bar represents 20 nm.

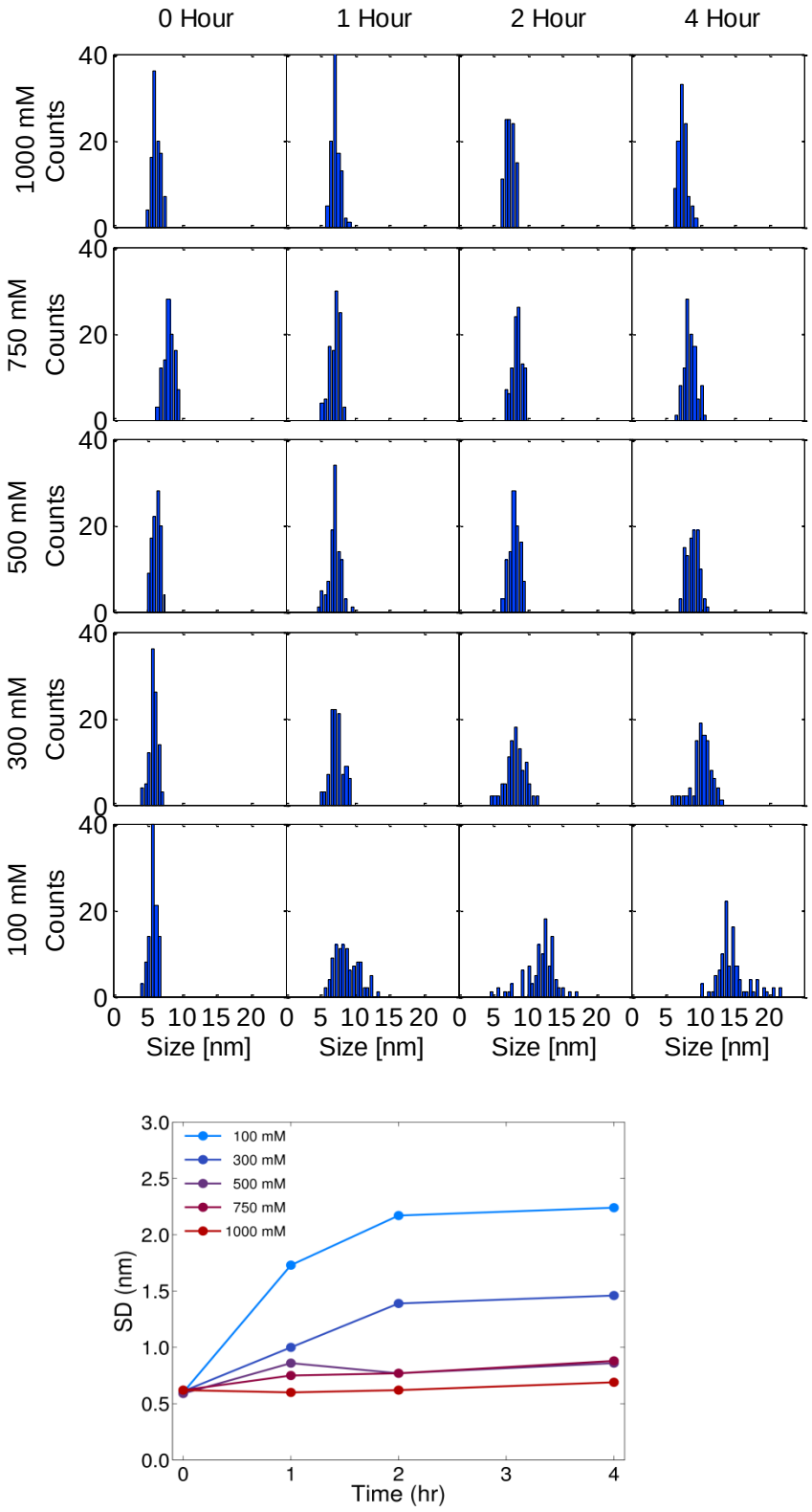

Figure S2: Top: Histograms of NP sizes measured from TEM image. A representative TEM for each histogram is shown in **Figure S1**. The mean and RSD (standard deviation/mean size) of these histograms are plotted in **Figure 3**. Bin size is 0.5 nm. **Bottom**: Size deviation of each aliquot over the duration of the soak.

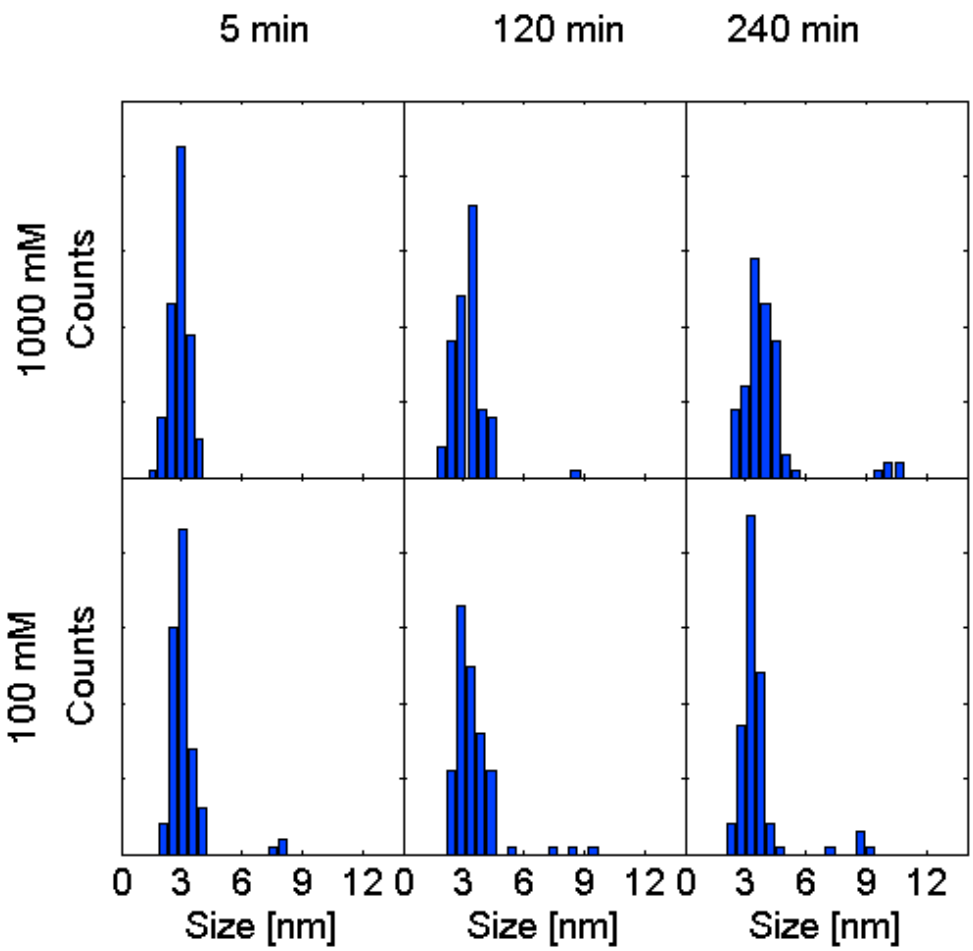

1000 mM	5 min	120 min	240 min
Size (nm)	2.9	3.2	3.7
RSD (%)	16	26	20
100 mM			
Size (nm)	3	3.3	3.4
RSD (%)	16	19	16

Figure S3: Histograms of the extended mixing stage at 50˚C for the highly concentrated (1000 mM) and conventional (100 mM) synthesis condition. Precursors are mixed at time equals zero and then soaked for 4 h at 50˚C with aliquots at 5 min, 120 min and 240 min. 100 particles are counted in determining the size and RSD of the NPs. Average size fluctuations are within measurement error. It should be noted within the conventional synthesis, there existed a few NPs with sizes of approximately 8 nm with no other intermediate sizes observed between the seeds (2-3 nm NP) and the large particles. Large particles are only observed within the highly concentrated reaction at 4 hr. These 8 nm particles are neglected in the determining of the size and RSD. Average and RSD are provide in table below.

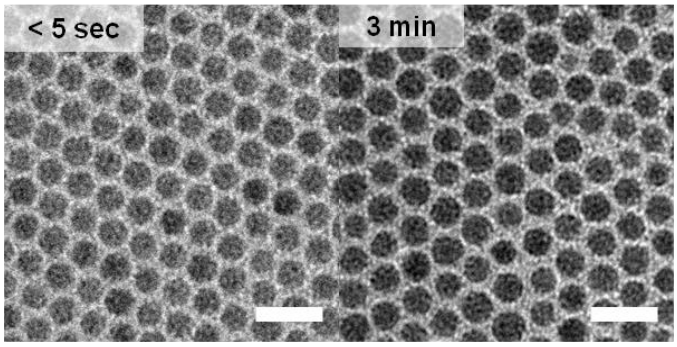

Figure S4: TEM images of the 2 hr aliquot of reactions with different injection speeds. The left image is the rapid injection of our typical reaction. The right image is a slow injection, in which ~ 0.05 mL is added every 10 sec over a 3 min period. The measured size of the fast and slow injection is 7.4 nm and 8.3 nm, respectively. Likewise, the RSD is 8.3% and 8.0%, respectively. Scale bar represents 20 nm.

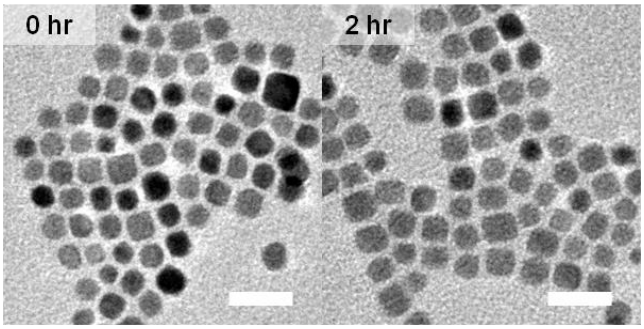

Figure S5: TEM images of PbS NPs at 0 hr and 2 hr of the soak at 185˚C. The NPs maintain a nearly constant size and quality through the reaction duration. The measured size and RSD at 0 hr is 7.0 nm and 17.5%, respectively. Similarly, at 2 hr, the size and RSD is 7.8 nm and 15.1%, respectively. Scale bar represents 20 nm.

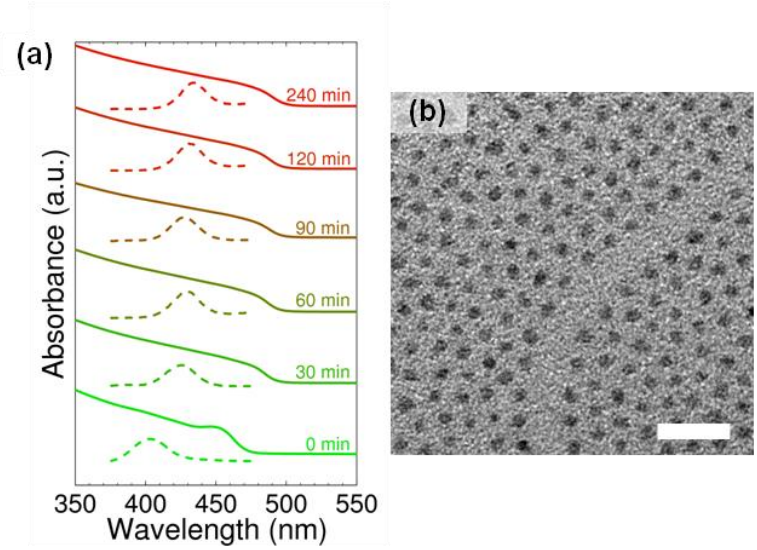

Figure S6: (a) Absorbance (solid) and PL (dotted) spectrum of a concentrated CdS reaction where a 2.5M TOP:S solution is injected into a 1.0M Cd-Oleate at 50˚C. The reaction is heated to 185˚C and aliquots are extracted every 30 min. After 30 min the absorbance edge stops shifting, indicative of halted NP growth. (b) TEM image of the reaction at 0 min into the soak. Scale bar represents 20 nm.

Replicate Experiments

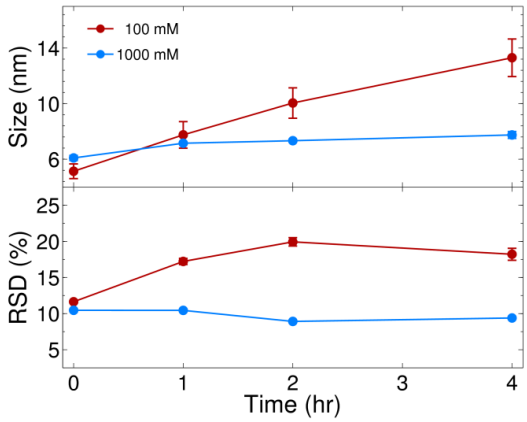

Figure S7. Replicate experiments (three experiments each) for the conventional (100 mM [CuCl]) and highly concentrated (1000 mM [CuCl]) reactions. Reactions are performed under similar conditions. The error bars are deviations between NP sizes at that time. Marker size is equivalent to a 5% deviation. NPs from the conventional reactions vary between experiments – associated with thermal fluctuations, i.e. different heating mantle and ambient conditions. NPs from the highly concentrated reactions are consistent (~5% deviation – error bars are small and are covered by markers). Concentrated systems are thermally more robust potentially due to lower thermal diffusivities. The error bars on the high concentrated conditions are smaller than the data points.

Dynamic Light Scattering

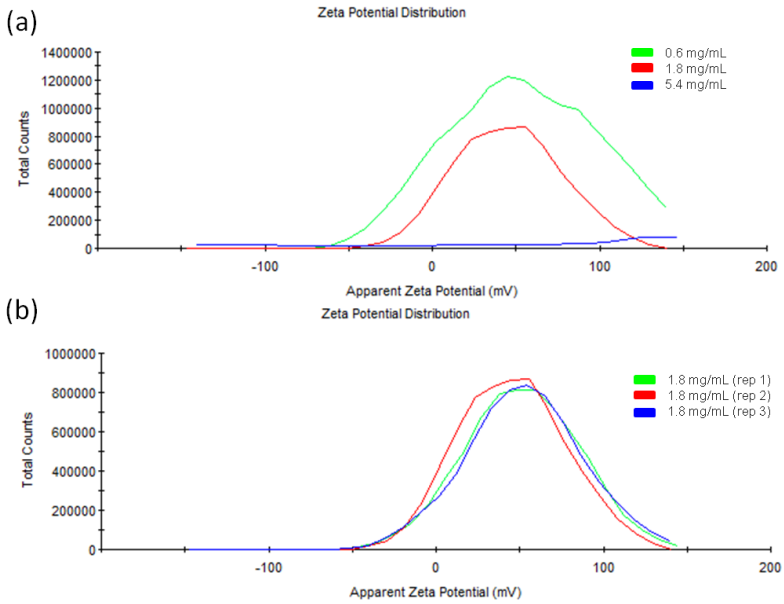

Figure S8: Dynamic Light Scattering (DLS) of cleaned NP from the concentrated (1000 mM) reactions. Samples were diluted in hexane in order to get accurate zeta potentials. The Huckel theory is used to predict the zeta potentials. (a) Various NP dilutions in hexane and (b) three replicates at concentration~1.8 mg NP/mL, that yield an average zeta potential of ~ +50 mV.

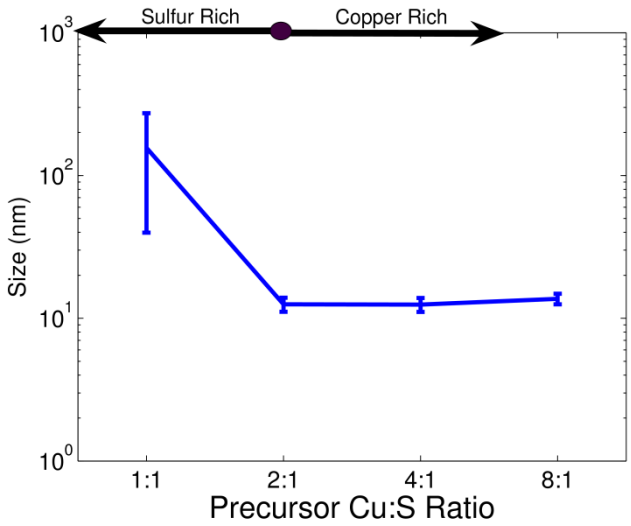

Figure S9: Reactions are performed at different Copper to Sulfur ratios, and a Cu:S ratio of 2:1 is stoichiometric. A Cu:S ratio of 1:1, or sulfur rich, yields large polydisperse particles. Reactions run at stoichiometric conditions or greater in copper content remain small. Increasing copper content also decreases poly-dispersity to a small degree. All NP sizes correlate to a 2 hr soak time.

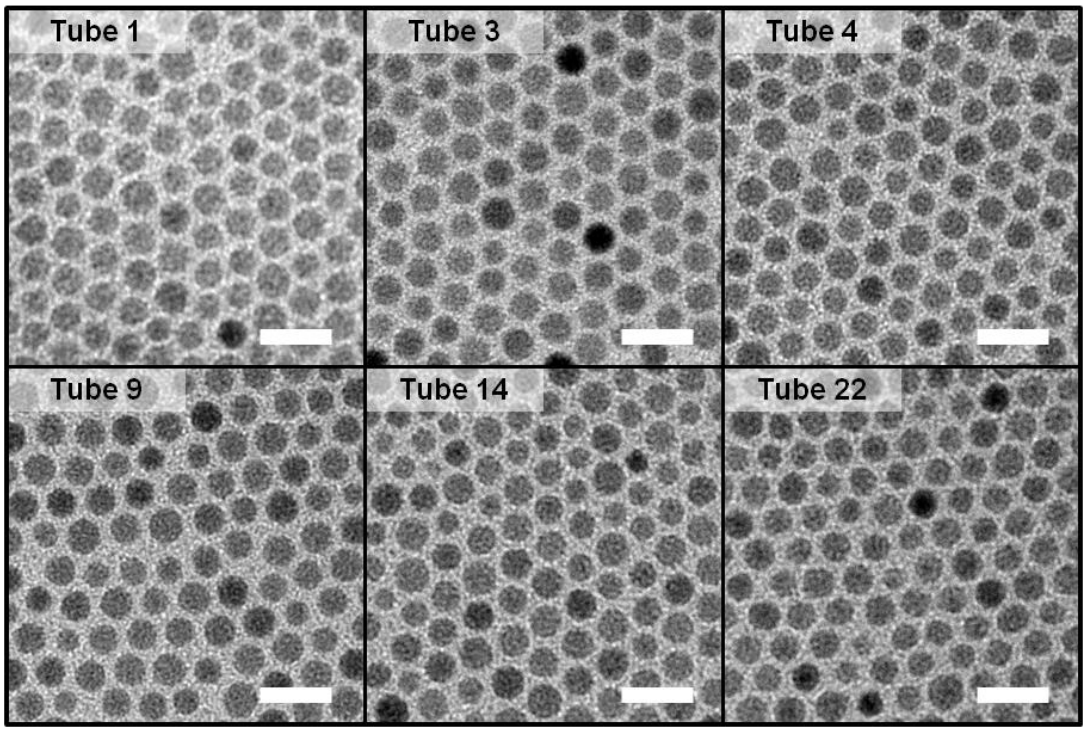

Figure S10: TEM images of randomly selected centrifuge tubes of the 2500 mL reaction cleaned at various times: 1)Tubes 1-8 were fully cleaned 2 hrs after quench, 2) Tubes 9-12 were fully cleaned 3 hrs after quench, Tubes 13-16 were fully cleaned 4 hrs after quench, 4) Tubes 17- 24 were fully cleaned 6 hrs after quench. Scale bar represents 20 nm.

XRD analysis

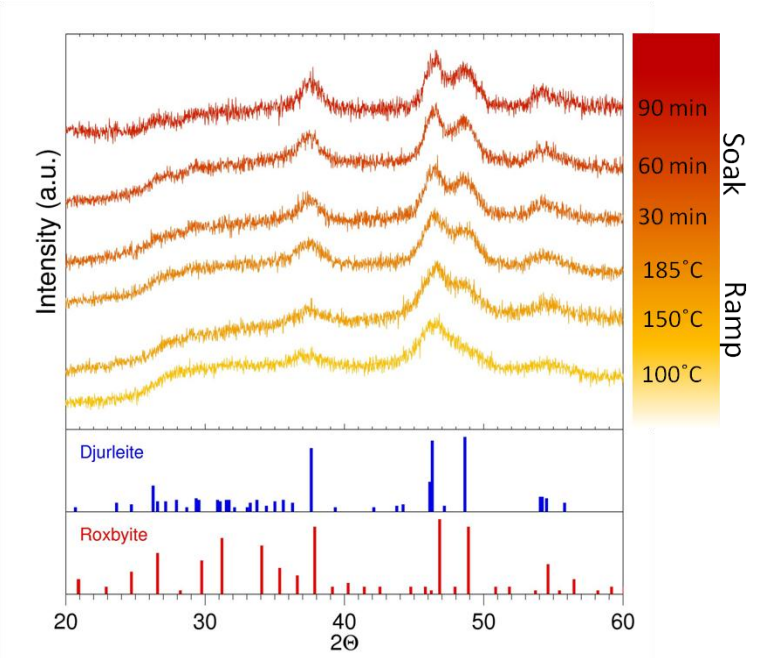

Figure S11: Series of XRD patterns from the same concentrated (1000 mM) reaction at various temperatures along the ramp and various times in the soak at 185˚C. The djurleite ($Cu_{31}S_{16}$, JCPDS: PDF#00-023-0959) and roxbyite (Cu_7S_4, JCPDS: PDF#00-023-0958) theoretical peaks are provided at the bottom. The NPs begin to crystallize during the ramping process and no longer crystallize during the soak.

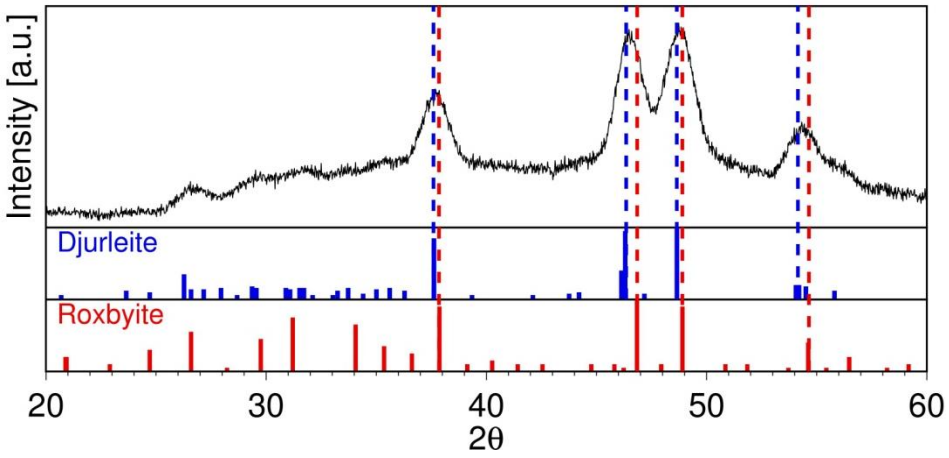

Figure S12: XRD pattern of 2500 mL reaction. The blue and red dotted lines correspond to the djurleite and roxbyite phase, respectively. The pattern is a mix between the djurleite phase ($Cu_{31}S_{16}$, JCPDS: PDF#00-023-0959) and the roxbyite phase (Cu_7S_4, JCPDS: PDF#00-023-0958).

Thermogravimetric Analysis

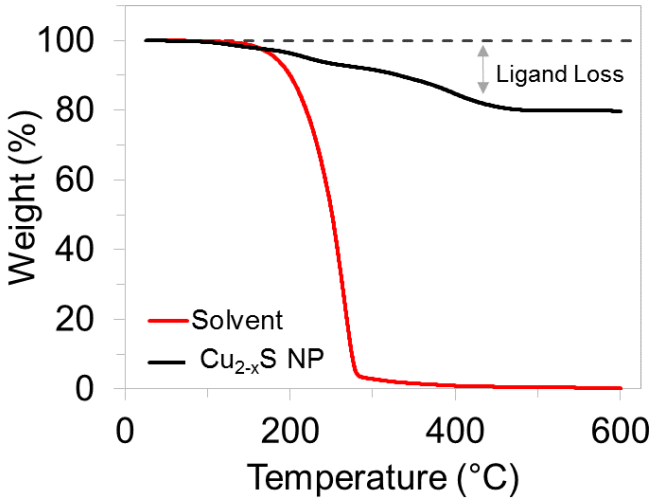

Figure S13: Thermogravimetric analysis (TGA) of large-scale synthesis product, compared to 80/30% OLA/ODE solvent. Only 20% of the large-scale product was ligand.

Viscosity Measurements

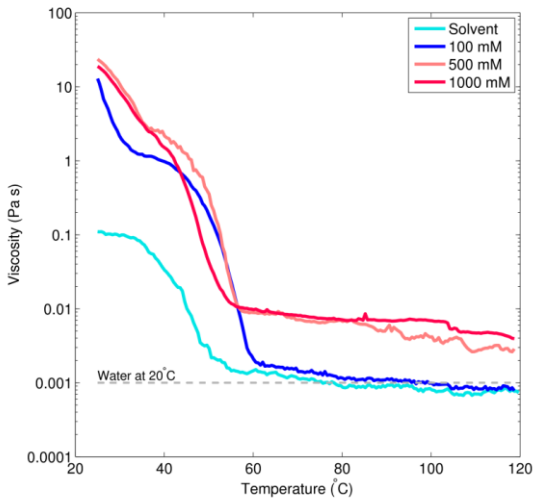

Figure S14: Viscosity measurements of the raw (unpurified) conventional (100 mM [CuCl]) reaction and the highly concentrated (1000 mM [CuCl]) reaction solutions between 25 to 120˚C are done using a parallel plate rheometer. The viscosity of the highly concentrated reaction is ~4 cP. The viscosity of the conventional reaction is ~0.8 cP. A water reference is given to provide a baseline for observational viscosity. Above 120˚C, the raw reaction solution beginnings to vaporize (and mass loss is visible in the TGA data, **Figure S13, S16**), impairing reliable viscosity measurements.

Thermal Spike Experiments

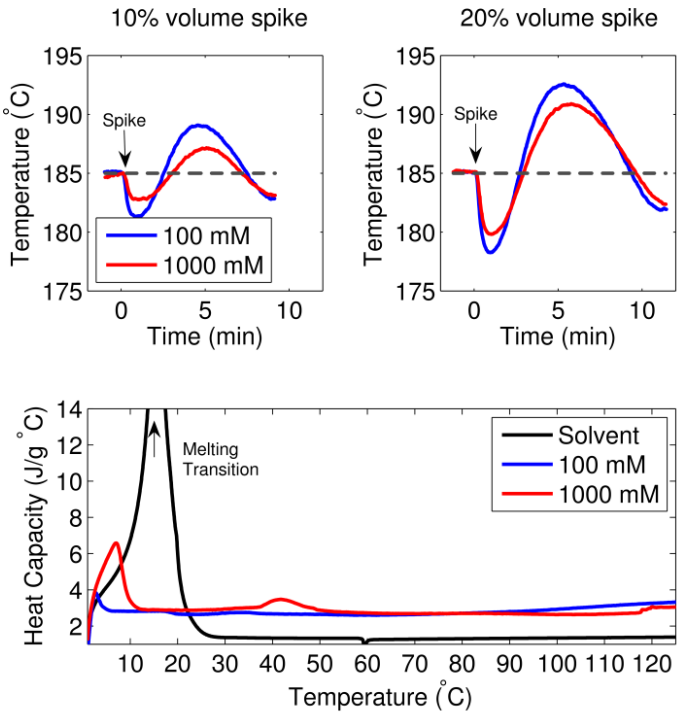

Figure S15: **Top**: Thermal spike experiment of the highly concentrated and conventional reaction. A 10 vol.% and a 20 vol.% solvent spike is injected into the NP solution at 185˚C. The initial spike and the subsequent oscillation is provided. A 2˚C and 4˚C temperature drop is observed with a 10 vol.% spike for the highly concentrated and conventional condition, respectively. The temperature drop is nearly doubled for each condition with a 20 vol.% spike. **Bottom**: Specific heats of 70/30% oleylamine/octadecene solvent, and the raw conventional and highly concentrated condition from differential scanning calorimetry (DSC). The heat capacity of the pure solvent is lower than that of the NP solutions. The highly concentrated condition has a slightly larger (factor of 2) specific heat than the conventional condition and therefore can retain heat its thermal energy or is less susceptible to thermal perturbation. The gradual rise in heat capacity above 80°C may be due to mass loss from the sample pan, which would inflate the heat capacity. Specific heat values at 50˚C are reported in **Table S3**.

Thermogravimetric analysis (TGA) of cleaned product

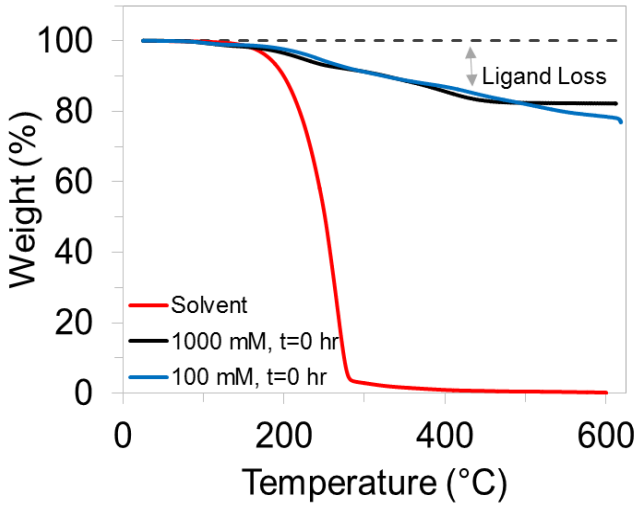

Figure S16: Thermogravimetric analysis (TGA) of cleaned conventional and highly concentrated product. Similar ligand lost is observed for both conditions, with a slightly higher ligand content in the conventional case. The mass loss is comparable to the large scale reaction in **Figure S13**. The OLA/ODE mixture is plotted for a reference to the solvent.

NP size evolution models

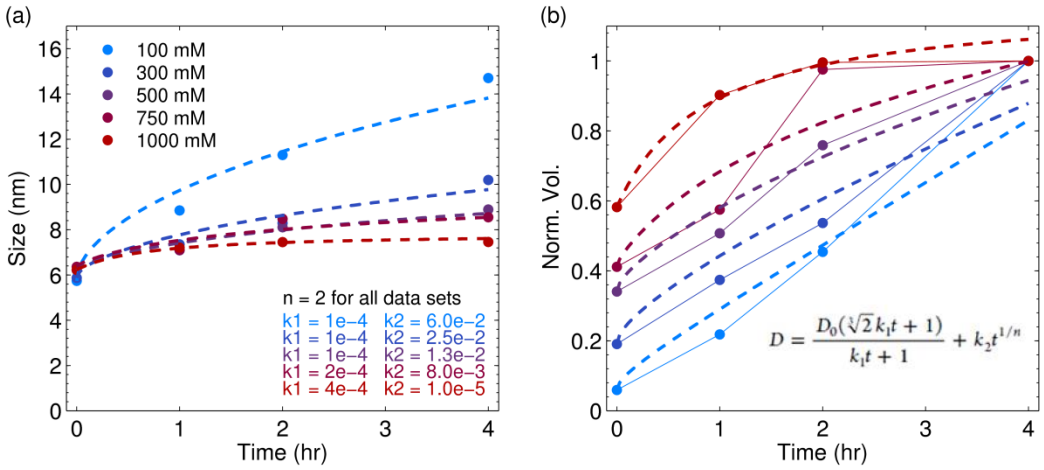

Figure S17: (a) Measured NP sizes from experiments at all concentrations fitted with a coupled oriented attachment (OA) and Ostwald ripening (OR) model proposed by Huang *et al.*[12] The fitting parameters are included within the graph and are arbitrarily fitted. (b) The particle sizes are converted to particle volumes to better understand how it fits the data. The equation used to fit the particle sizes is provided in this graph; where the first term in the expression is the OA rate and the second is the OR rate. Interestingly, the value of k_2 drops substantially as the concentration of the reaction increase, which is supportive of their linear volumetric growth. On the other hand, k_1 or OA rate for each concentration remains small and nearly constant, suggests the growth from this process is small, yet in the high concentrations (750 and 1000 mM) k_1 becomes prominent. The fitted volumes are based on a simply sphere volume and then normalized with the particle volume at 4 hour. The R^2 suggests the Huang

models fits the data well (R^2 near 1), but observationally, the fits do not converge to 1 when normalized by the experimental data at 4 hrs. See **Table S5** for R^2 values fit comparisons.

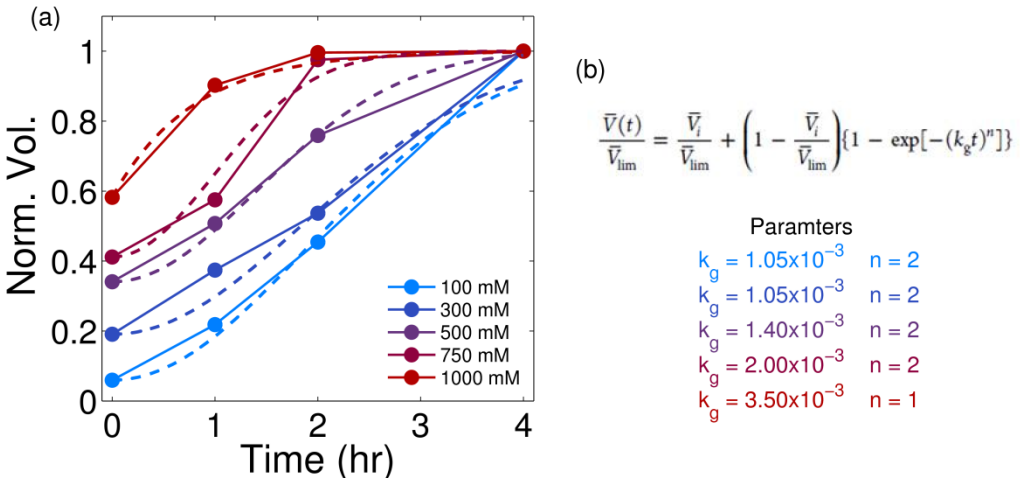

Figure S18: (a) Particle volumes fitted with the KJMA model (dashed lines)[13]. (b) The KJMA equation used to fit the data in terms of normalized volume, where V_{lim} is the particle volume at 4 hrs. The fitting parameters are provided below the equation and are color coded to the reaction concentrations. The model is designed to fit sigmoidal growth curves, in which monomer addition or coalescence is dominant (k_g). This model does not capture the Ostwald ripening phenomena. In comparison to the other discussed models, the fits here have the greatest R^2 values for the entire concentration span. However, there is very little meaning behind each fitting parameter (*e.g.* n is an arbitrary value and k_g is a lumped growth rate). See **Table S5** for R^2 values fit comparisons.

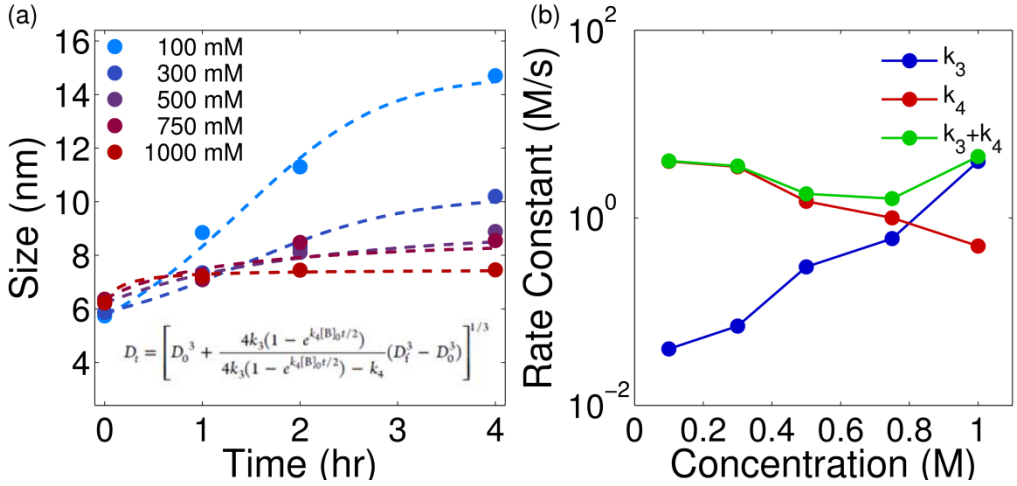

Figure S19: NP size fitting model proposed by Finney *et. al.*[14] (a) The model is fit the particle sizes shown in **Figure 3**, **Figure S1** and **Figure S2**. The equation used to fit the data is included within the graph. An example particle concentration, [B] is calculated below in the sample calculation section of this document. (b) The rate constant fitting parameters k_3 and k_4 are the bimolecular (coalescence) and the autocatalytic rate (Ostwald ripening) rates, respectively. The increase in k_3 with increasing precursor (salt) concentration is related to the increased screening of the greater anion concentration. This effectively reduces repulsive forces between particles, enabling them to collide more frequently. Similarly, higher anion concentration increases the probability of surface bound ions, which stabilize the particle surface and therefore reduce its reactivity to other particles. This effectively would reduce the autocatalytic rate, k_4. See **Table S5** for R^2 values fit comparisons.

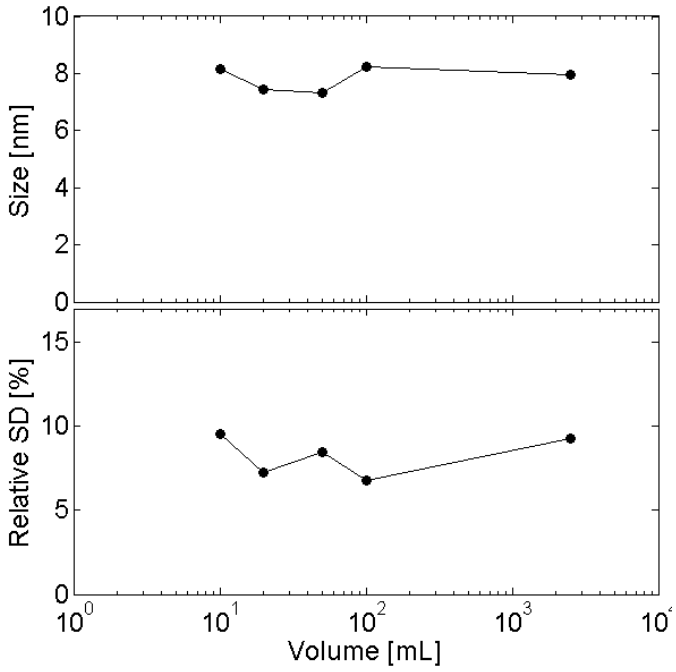

Figure S20: Highly concentrated reactions performed at different volumes covering 3 orders of magnitude (10 mL to 2500 mL). NPs for each reaction are similar in size.

Sample calculations

Stokes-Einstein-Sutherland relation of viscosity and diffusivity

D is mass diffusivitiy, k_b is Boltzmann's constant, T is temperature, η is shear viscosity, and r is the NP radius.

$$Mass\ Diffusivity = D = \frac{k_b\, T}{6\,\pi\,\eta\,r}$$

$$D = \frac{1.38 \cdot 10^{-23}\frac{J}{K} \cdot (120 + 273.15)K}{6\,\pi\,0.0038\,mPa \cdot s \cdot \left(\frac{5.5}{2}\right) \cdot 10^{-9}\,m} = 2.8 \cdot 10^{-11}\frac{m^2}{s}$$

Thermal Diffusivity

k is the thermal conductivity, ρ is mass-average density, C_p is the specific heat, and ρC_p is equivalent to the volumetric heat capacity. We assumed a constant thermal conductivity for all concentration. The thermal conductivity for salts and oils are similar and therefore different mass fractions do not alter the value much.

$$Thermal\ Diffusivity = \alpha = \frac{k}{\rho C_p}$$

$$\alpha = \frac{0.13\frac{W}{m\cdot K}}{2.9\frac{J}{m\cdot K}\left(0.9\cdot 813\frac{kg}{m^3} + 0.1\cdot 5600\frac{kg}{m^3}\right)} = 5.2 \cdot 10^{-8}\mathrm{m}^2/\mathrm{s}\,.$$

Molar Concentration of Particles

[P] is the concentration of Cu_2S at full conversion, MW is the molecular weight f Cu_2S, ρ is the density, V_p is the particle volume at the beginning of the soak, and N_A is Avogadro's Number.

$$Particle\ Concentration = \ [B] = \frac{[P]MW_{Cu_2S}}{\rho V_p N_A}$$

$$[B] = \frac{0.5\frac{mol}{L} \cdot 159.2\frac{g}{mol}}{5600\frac{g}{L} \cdot 125\frac{nm^3}{\#} \times 10^{-24}\frac{L}{nm^3} \cdot 6.022 \times 10^{23}\frac{\#}{mol}} = 188\mu M\ of\ Particles$$

Smoluchowski Collision Frequency[11]

R is the diameter of the NP, D is the diffusivity of the particle, and [B] is the concentration of particles in #/volume. Values for other concentrations are provided in **Table S4**

$$Collision\ Frequency = \ Z = 4\pi RD[B]$$

$$Z = 4\pi \cdot 6.2 \times 10^{-9}nm \cdot 2.8 \times 10^{-11}\frac{m^2}{s} \cdot 1.1 \times 10^{23}\frac{\#}{m^3} = 2.5 \times 10^5\frac{\#}{s}$$

Yield Calculations

$$Theoretical\ Yield = \frac{m_{CuCl}}{M_{w_{CuCl}}} \cdot M_{w_{Cu_2S}} \cdot v$$

where m_{CuCl} is the initial is mass of CuCl, $M_{w_{CuCl}}$ and $M_{w_{Cu_2S}}$ are the respective molecular weights for CuCl and Cu_2S, respectively, and v is the molar ratio of Cu_2S to CuCl.

$$Theoretical\ Yield = \frac{1\ g}{98.999\frac{g}{mol}} \cdot 159.16\frac{g}{mol} \cdot \frac{1\ mol\ Cu_2S}{2\ mol\ CuCl} = 0.803\ g$$

$$Yield\ Percent = \frac{Collected\ Mass\ \cdot (100\% - wt\%\ ligand)}{Theoretical\ Yield}$$

$$Yield\ Percent = \frac{08644\ g \cdot (100\% - 17.8\%)}{0.803\ g} = 88\%$$

Residual Precursor Calculation

Equations

$$Residual\ Precursor\ Mass = Theoretical\ Yield - Collected\ Mass\ \cdot (100\% - wt\%\ ligand)/100$$

$$Residual\ Precursor\ Concentration = \frac{Residual\ Precursor\ Mass}{Solution\ Volume \cdot M_{w Cu_2S}}$$

The change in volume by adding residual precursor mass to existing particles is

$$Change\ in\ Volume\ = Vol_{part} \cdot \left(\frac{1}{Yield\ Percent\ /\ 100\%} - 1\right)$$

$$NP\ Diameter\ at\ 100\%\ conversion\ = 2\left(\frac{Change\ in\ Volume \cdot 3}{4\pi} + Initial\ NP\ radius^3\right)^{\frac{1}{3}}$$

Calculation

$$Residual\ Precursor = 0.803g - 0.8644\ g \cdot (100\% - 17.8\%)/100 = 0.093\ g$$

$$Residual\ Precursor\ Concentration = \frac{0.093g}{0.011\ mL \cdot 159.16 \frac{g}{mol}} = 53\ mM$$

Using initial NP diameter of 6nm and 88% yield,

$$Change\ in\ Volume\ = \frac{4}{3}\pi\left(\frac{6\ nm}{2}\right)^3 \cdot \left(\frac{1}{\frac{88\%}{100\%}} - 1\right) = 15.4\ nm^3$$

$$NP\ Diameter\ at\ 100\%\ conversion\ = 2\left(\frac{15.4\ nm^3 \cdot 3}{4\pi} + (3\ nm)^3\right)^{\frac{1}{3}} = 6.3\ nm$$

Step and Living Coalescence Models

The theoretical distributions for the step and living coalescence models shown in **Figure 7** were obtained simulating the coalescence of initial size distribution at t = 0 hr (~6 nm;RSD=10%). An initial particle distribution is generated using the NP size and standard deviation at the beginning of the soak for the conventional and highly concentrated conditions. Then, NP are randomly selected and combined by a volume sum. The new particle size is then computed and the total particle count is reduced by one per combination event. In the case of step coalescence, a selected particle will be rejected if it has already coalesced, and another particle that has not coalesced will be selected. This process is repeated until every particle has coalesced. Then, this process begins again for the next distribution shift (I, II, III, etc.). Each distribution shift (e.g., curve I to II) corresponds to the point when the number of particles has been cut in half. For the case of living coalescence, the process is similar, except particles are not rejected if they have already coalesce (and not all particles will coalesce), and the particles are allowed to coalesce again. For step coalescence, this means each particle experiences one coalescence event between I and II while for living coalescence each particle may undergo a range of coalescence events (from none to many).

References

(1) Yang, Y. A.; Wu, H.; Williams, K. R.; Cao, Y. C. *Angew. Chemie - Int. Ed.* **2005**, *44*, 6712–6715.
(2) Lotfipour, M.; Machani, T.; Rossi, D. P.; Plass, K. E. *Chem. Mater.* **2011**, *23*, 3032–3038.
(3) Hendricks, M. P.; Campos, M. P.; Cleveland, G. T.; Plante, I. J.; Owen, J. S. *Science* **2015**, *348*, 1226–1230.
(4) Chan, E. M.; Xu, C.; Mao, A. W.; Han, G.; Owen, J. S.; Cohen, B. E.; Milliron, D. J. *Nano Lett.* **2010**, *10*, 1874–1885.
(5) Zhang, H.-T.; Wu, G.; Chen, X.-H. *Langmuir* **2005**, *21*, 4281–4282.
(6) Joo, J.; Na, H. Bin; Yu, T.; Yu, J. H.; Kim, Y. W.; Wu, F.; Zhang, J. Z.; Hyeon, T. *J. Am. Chem. Soc.* **2003**, *125*, 11100–11105.
(7) Jackson, F. G. *J. Am. Chem. Soc.* **1912**, *34*, 1470–1480.
(8) Wrenick, S.; Sutor, P.; Pangilinan, H.; Schwarz, E. E. In *Proceedings of WTC2005, World Tribology Congress III*; Washington, D.C., USA, **2005**, 1–2.
(9) Regel, A. R.; Smirnov, I. A.; Shadrichev, E. V. *Phys. Stat. Sol.* **1971**, *13*, 13–57.
(10) Sangeetha, N. M.; Gauvin, M.; Decorde, N.; Delpech, F.; Fazzini, P. F.; Viallet, B.; Viau, G.; Grisolia, J.; Ressier, L. *Nanoscale* **2015**, 12631–12640.
(11) Chan, E. M.; Marcus, M. A.; Fakra, S.; ElNaggar, M.; Mathies, R. A.; Alivisatos, A. P. *J. Phys. Chem. A* **2007**, *111*, 12210–12215.
(12) Huang, F.; Zhang, H.; Banfield, J. F. *J. Phys. Chem. B* **2003**, *107*, 10470–10475.
(13) Shields, S. P.; Richards, V. N.; Buhro, W. E. *Chem. Mater.* **2010**, *22*, 3212–3225.
(14) Finney, E. E.; Shields, S. P.; Buhro, W. E.; Finke, R. G. *Chem. Mater.* **2012**, *24*, 1718–1725.
(15) Wang, F.; Richards, V. N.; Shields, S. P.; Buhro, W. E. *Chem. Mater.* **2014**, *26*, 5–21.